The Company of
Biologists

RESEARCH ARTICLE

Astrocyte-intrinsic and -extrinsic *Fat1* activities regulate astrocyte development and angiogenesis in the retina

Françoise Helmbacher*

ABSTRACT

Angiogenesis is a stepwise process leading to blood vessel formation. In the vertebrate retina, endothelial cells are guided by astrocytes migrating along the inner surface, and the two processes are coupled by a tightly regulated cross-talks between the two cell types. Here, I have investigated how the FAT1 cadherin, a regulator of tissue morphogenesis that governs tissue cross-talk, influences retinal vascular development. Late-onset *Fat1* inactivation in the neural lineage in mice, by interfering with astrocyte progenitor migration polarity and maturation, delayed postnatal retinal angiogenesis, leading to persistent vascular abnormalities in adult retinas. Impaired astrocyte migration and polarity were not associated with alterations of retinal ganglion cell axonal trajectories or of the inner limiting membrane. In contrast, inducible *Fat1* ablation in postnatal astrocytes was sufficient to alter their migration polarity and proliferation. Altogether, this study uncovers astrocyte-intrinsic and -extrinsic *Fat1* activities that influence astrocyte migration polarity, proliferation and maturation, disruption of which impacts retinal vascular development and maintenance.

KEY WORDS: Angiogenesis, Astrocytes, Fat cadherins, Retina, Planar polarized migration

INTRODUCTION

The vascular system is dedicated to the distribution of nutrients and oxygen to all organs, and serves as a vector for hormonal control and immune surveillance. Assembly of the vascular system involves a process called angiogenesis, by which endothelial cells coalesce to form vessels, which are subsequently remodeled in order to adapt blood flow to tissue scale. Whereas the cellular and molecular mechanisms underlying these processes are common to many organs (Ruhrberg and Bautch, 2013), some vascular properties are adjusted in an organ-specific manner, owing to tissue-specific cross-talks between endothelial cells and organ-specific cellular players. The retina represents an excellent system for studying the interactions between ECs and organ-specific cells, such as astrocytes or neurons.

In the mouse retina, angiogenesis starts after birth, with a phase (between P0 and P7) of horizontal vascular growth, in the plane of the inner-most retinal layer [sharing space with axons of retinal ganglion cell (RGC) neurons, which migrate towards the optic nerve]. This process is followed by a phase of perpendicular vessel

Aix Marseille Univ, CNRS, IBDM UMR 7288, Parc Scientifique de Luminy, Case 907, 13288 Marseille, France.

*Author for correspondence (francoise.helmbacher@univ-amu.fr)

F.H., 0000-0001-6822-1246

growth towards deeper retinal layers (between P7 and P21), resulting in the formation of additional vascular layers (Paredes et al., 2018; Ruhrberg and Bautch, 2013). During the horizontal phase, endothelial cells (ECs) are preceded by migrating astrocyte progenitor cells (APCs), which enter the retina through the optic nerve (Watanabe and Raff, 1988) and spread radially on the inner surface, reaching the retinal edges in a few days, ahead of EC migration (Tao and Zhang, 2014). A tight coupling of these two migratory waves is ensured by reciprocal signals exchanged by astrocytes and ECs. The astrocyte layer serves as substrate and guidance cue for migrating ECs. Ahead of the EC migration front, hypoxia induces immature astrocytes to secrete vascular endothelial growth factor (VEGF) (Stone et al., 1995), a chemo-attractant that promotes EC migration, signaling via VEGFRs (Gerhardt et al., 2003). As ECs migrate and newly formed vessels expand, the rise in oxygen level resulting from blood perfusion promotes astrocyte maturation, characterized by increased levels of the astrocyte marker glial fibrillary acidic protein (GFAP) and reduced VEGF levels (West et al., 2005). This oxygen-mediated silencing of VEGF expression in EC-covered astrocytes (proximal to the vascular front) is countered by the high VEGF levels induced by hypoxia in the EC-free distal region (Duan et al., 2017, 2014; Rattner et al., 2019; Stone et al., 1995). This establishes a VEGF gradient (high in distal immature astrocytes and low in proximal mature astrocytes), determining the outward direction polarity of EC migration (West et al., 2005).

Because of this mutual dependency, molecular alterations that interfere with astrocyte migration also impact on retinal angiogenesis progression (Duan et al., 2017, 2014; Kautzman et al., 2018; Lavina et al., 2018; Tao and Zhang, 2016), and manipulations interfering with EC migration compromise astrocyte maturation (Morita et al., 2017). Thus, astrocyte/EC coupling is indirectly influenced by the combination of intrinsic and extrinsic factors that modulate astrocyte migration. Among those, the substrates onto which astrocytes progress provide biochemical and physical cues that promote migration and instruct directions. A key secreted motility factor is PDGF, which is released by RGC neurons and signals via PDGFRα (Fruttiger et al., 1996). Another way in which RGC neurons instruct astrocytes is via their radially oriented axons, which physically constrain the outward migration direction (O'Sullivan et al., 2017). The inner limiting membrane (ILM), a layer of extracellular matrix (ECM) mainly produced by Müller glia and delimiting the border with the vitreous cavity (Halfter et al., 2008), constitutes another migration substrate. Mutations that alter ILM integrity, such as those inactivating ECM components (Edwards et al., 2010, 2011; Gnanaguru et al., 2013) or ECM receptors (Clements et al., 2017; Tao and Zhang, 2016), compromise astrocyte migration and retinal angiogenesis, and lead to vitreoretinopathies. Finally, astrocyte migration represents a perfect example of collective/planar polarized migration, and, as such, involves all the molecular pathways by which migrating cells

inform each other of their polarity, shape changes and speed, to fine-tune their collective behavior (Davey and Moens, 2017; Mayor and Etienne-Manneville, 2016).

My colleagues and I have previously reported that deletion of the *Fat1* cadherin gene causes abnormalities of the retinal vasculature (Caruso et al., 2013). However, the exact role played by *Fat1* had not been elucidated. Fat-like cadherins are known regulators of tissue morphogenesis, which are capable of modulating cell polarity, migration, growth and fate decisions (Blair and McNeill, 2018; Horne-Badovinac, 2017; Sadeqzadeh et al., 2014). Their binding to Dachsous cadherins triggers bidirectional signaling cascades impinging on the planar cell polarity (PCP) and Hippo/YAP pathways, influencing cytoskeletal dynamics and fate decisions both cell- and non-cell-autonomously (Blair and McNeill, 2018). Both the Hippo/YAP (Kim et al., 2017; Nakajima et al., 2017; Sakabe et al., 2017; Wang et al., 2017) and the PCP (Cirone et al., 2008) pathways are known modulators of angiogenesis. *Fat1* and *Yap* are involved in eye morphogenesis, and their inactivation similarly causes a congenital malformation called coloboma (Lahrouchi et al., 2019; Williamson et al., 2014). Fat/Dachsous and PCP signaling also coordinate polarized migration (Horne-Badovinac, 2017). I recently illustrated how *Fat1* coordinates polarized migration and differentiation of myogenic progenitors through complementary activities in several cell types (Helmbacher, 2018). Thus, postnatal retinal angiogenesis, with two polarized migration events coupled to one another, and with known involvement of FAT/PCP signaling, represents another logical place where *Fat1* can coordinate morphogenesis.

Here, I have explored how *Fat1* influences retinal vascular development in mice. In the postnatal retina, *Fat1* is predominantly expressed in astrocytes and Müller glia. Its deletion in the neural lineage was first achieved with a late-onset CRE driver that bypassed its early morphogenetic activity, thereby rescuing the coloboma found in constitutive knockouts. Neural-specific deletion resulted in altered astrocyte migration polarity at the leading edge, subsequently interfering with astrocyte maturation, as manifested by lowered GFAP and PDGFRα levels, and with horizontal vascular progression rate. Abnormalities of the vascular architecture persisted at adult stages in neural-specific *Fat1* mutants. The altered astrocyte polarity occurring at postnatal stages resulted neither from alterations of ILM integrity nor from aberrant axonal trajectories, but was reproduced in a genetic setting that allows inducible *Fat1* deletion in migrating astrocyte progenitors. Thus, *Fat1* activity is required in migrating astrocyte progenitors to coordinate their polarity and subsequent maturation.

RESULTS
Constitutive Fat1 disruption impairs eye cup morphogenesis and optic fissure closure
The present study aimed to investigate how *Fat1* gene activity in the postnatal neural lineage influences retinal angiogenesis. However, *Fat1* disruption affects optic cup development, resulting in morphological eye abnormalities, with varying severity and penetrance, ranging from microphthalmic eyes to normally shaped eyes with vascular phenotypes (Caruso et al., 2013; Ciani et al., 2003; Lahrouchi et al., 2019; Sugiyama et al., 2015). Such a wide range of phenotypic severity implies that *Fat1* is required at several stages, with incomplete phenotypic penetrance of knockout alleles for each of these functions. Assessing eye and retinal morphology from E12.5 to E14.5 in *Fat1*-deficient embryos, confirmed the range of known phenotypes (Fig. 1). These included ventral coloboma: a congenital malformation of the retina representing a major cause of

childhood blindness (Bovolenta and Martinez-Morales, 2019; Chang et al., 2006). Coloboma results from the failure of a morphogenetic process called ventral closure, during which the ventral edges of the optic cup align (forming the optic fissure) and fuse, ensuring continuity of the ventral retina (Chang et al., 2006; Fuhrmann, 2010; Morcillo et al., 2006). Defective ventral closure causes the optic cup to remain open ventrally.

At E12.5, near ventral closure completion, control embryos exhibited a nearly closed eye cup, with the pigmented ventral edges closely apposed against each other (Fig. 1A). At that stage, the eye size (area relative to trunk length) was only modestly reduced in most *Fat1*$^{-/-}$ embryos (17/23), whereas a small proportion (6/23) exhibited severe reduction in optic cup size (microphthalmia) (Fig. 1A,E). In the *Fat1*$^{-/-}$ embryos with normal eye size, the optic fissure nevertheless failed to close, resulting in a coloboma characterized by an increased ventral groove width (Fig. 1A,F), also distinguishable on posterior coronal sections (Fig. 1C), with mesenchymal tissue abnormally located in the groove of *Fat1*$^{-/-}$ optic cups. This phenotype persisted beyond E14.5 (Fig. 1B), indicating a failure rather than a delay in the ventral closure process. Thus, *Fat1* activity is required for optic fissure closure, a role recently shown to be evolutionarily conserved, as *Fat1* loss-of-function mutations lead to coloboma not only in mouse, but also in zebrafish and human (Lahrouchi et al., 2019).

Delayed Fat1 ablation in the neural lineage bypasses early eye morphogenesis defects
With such disrupted eye morphogenesis, the constitutive knockout is unsuitable for studying potential *Fat1* involvement at later stages. Assessing its requirement for postnatal processes requires deleting *Fat1* only after completion of eye morphogenesis. Although predominant in the mesenchyme just below the eye cup, *Fat1* is also expressed in the ciliary margin of the neural retina and in the RPE (Fig. 1D), as seen by following expression of a *Fat1*^{LacZ} allele in E12.5 embryo sections. Each of these components may contribute to eye growth and ventral closure. This phenotype was suggested to result from *Fat1* activity in the RPE (Lahrouchi et al., 2019). This raises the possibility that retina-specific deletion at an early stage could potentially be detrimental for eye morphogenesis. To circumvent this and produce mutant retinas without morphological abnormality, I used the *Nestin-cre* line, which allows neural-specific CRE-mediated excision, but with a late onset in some regions resulting in delayed recombination compared with most other neuronal areas (Lamballe et al., 2011; Tronche et al., 1999). My colleagues and I have previously shown that *Nestin-cre*-driven deletion of the HGF receptor gene *Met* only reached complete excision in spinal motor neurons at E13.5, allowing early function to be preserved in order to assess its role at later stages (Lamballe et al., 2011). Likewise, late *Nestin-cre* activity in the retina may be suited to ablating neural *Fat1* expression late enough to preserve its putative activities during eye cup morphogenesis.

To determine the timing of *Nestin-cre*-mediated activity in the developing optic cup, I evaluated recombination efficiency with a *R26-YFP* recombination reporter (Srinivas et al., 2001), in which YFP expression, driven by the ubiquitous R26 locus, is conditioned by CRE-mediated deletion of a Lox-STOP-Lox cassette, allowing lineage tracing. I followed the pattern of YFP expression in *Nestin-cre*; *R26*$^{YFP/+}$ retinas at different stages. At E13.5, 1 day after completion of the morphogenetic events governing optic fissure fusion, although YFP expression outlined the whole central nervous system (CNS), little fluorescence was detected in the eye (Fig. 2A). YFP immunohistochemistry on sections confirmed robust YFP
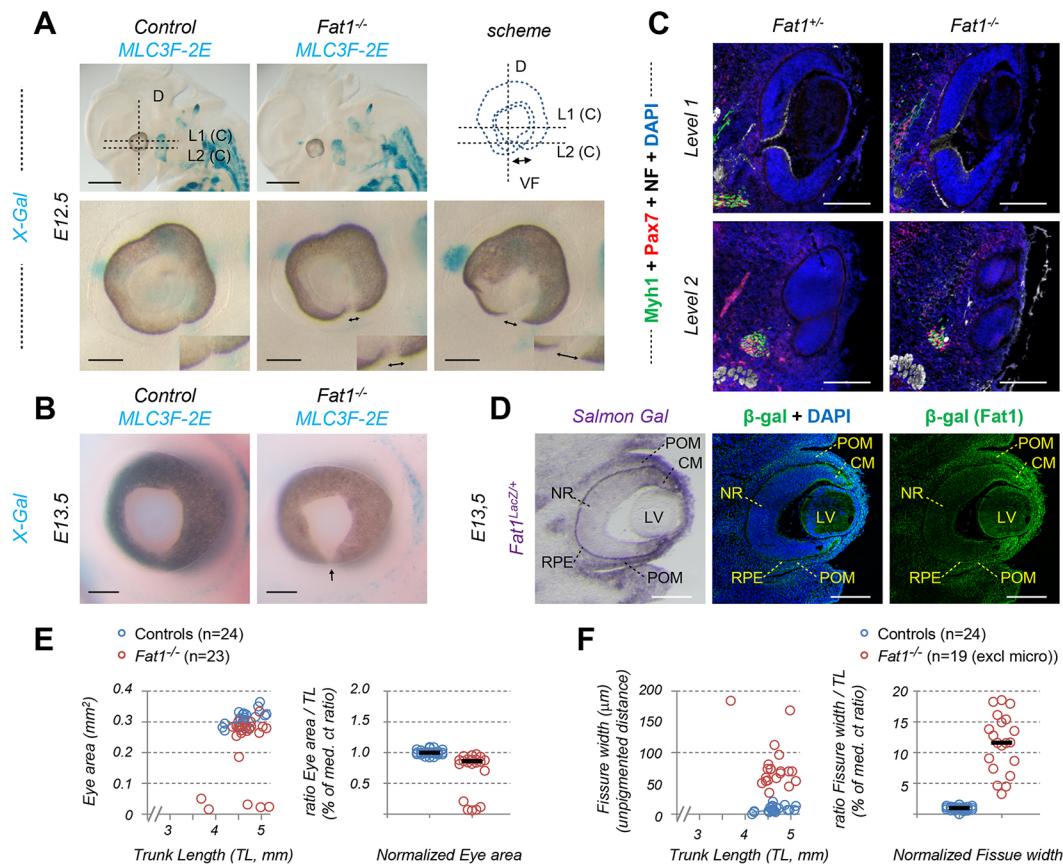
Fig. 1. Fat1 disruption causes a ventral Coloboma phenotype. (A,B) Eye morphology was analyzed on whole-mount control or $Fat1^{-/-}$ embryos at E12.5 (A) and E13.5 (B), with muscles highlighted by the *Mlc3F-2E* transgene. Arrow in B indicates a typical coloboma. (C) Immunohistochemistry analysis of retinas in wild-type and $Fat1^{-/-}$ embryos at E12.5 on horizontal sections at two levels (dotted lines labeled L1 and L2 in A), with DAPI (blue), anti-neurofilament (white), anti-Pax7 (red) and anti-Myh1 (green). (D) *Fat1* expression is visualized by Salmon gal staining (left), or by anti-β-galactosidase (middle and right) immunostaining on neighboring coronal sections of a $Fat1^{LacZ/+}$ E13.5 embryo (vertical dotted line in A). (E,F) Quantifications of eye area (EA, E) and ventral fissure width (VFW, F), relative to trunk length (TL), plotted as raw data (left plots) or normalized ratios (EA/TL or VFW/TL, relative to median ratio of controls; right plots). CM, ciliary margins; I, lens; NR, neural retina; POM, peri-ocular mesenchyme; RPE, retinal pigmented epithelium. Scale bars: in A, 1 mm (top); 200 μm (bottom); in B-D, 200 μm.

expression in a large fraction of the CNS, and in almost all cells of the proliferative epithelium of the lens vesicle (Fig. 2A, middle panels), but revealed that recombination activity in the E13.5 optic cup itself was limited to a few cells in the ventral RPE, and completely absent in the neural retina (Fig. 2A, top right). Thus, at E13.5, *Nestin-cre*-driven recombination in the eye is restricted to the lens epithelium and ventral RPE, but absent from the neural retina, in contrast to the robust recombination already achieved in the CNS. *Nestin-cre* activity only started to be detectable in the neural retina at E16.5, with YFP+ cells in several retinal layers encompassing glia and neurons (Fig. 2A, bottom), indicating ongoing CRE-mediated deletion, and near-complete recombination in the lens. The extent of *Nestin-cre*-mediated deletion reached 100% efficiency at adult stage in Müller glia cells, with a complete overlap between YFP and glutamine synthetase (GS, *Glul* gene) signals, and in astrocytes (labeled with GFAP antibodies) (Fig. 2B).

As expected, this late onset of *Nestin-cre* activity in the retina allowed the preservation of *Fat1* morphogenetic activity until completion of optic fissure closure, making it unlikely that *Nestin-cre*-driven *Fat1* deletion could interfere with optic cup morphogenesis. This approach indeed resulted in normally shaped eyes in *Nestin-cre; Fat1$^{Flox/Flox}$* at E12.5 and E13.5 (Fig. 2C,D). In conclusion, this genetic setting (later referred to as *Fat1^{Nestin}*; see Materials and Methods) is suitable to study later roles of *Fat1* in the

neural retina without interfering with early eye morphogenesis and with other non-neural functions (Caruso et al., 2013; Ciani et al., 2003; Gee et al., 2016; Helmbacher, 2018). Such a strategy helped demonstrate that a neural source of VEGF-A was required in a dose-dependent manner for retinal vessel morphogenesis (Haigh et al., 2003).

Fat1 expression in the postnatal retina

I next explored *Fat1* expression in the retina during postnatal vascular morphogenesis (Fig. 3, Fig. S1), using a *Fat1^{LacZ}* knock-in allele (Caruso et al., 2013; Helmbacher, 2018). In flat-mounted retinas from P3 *Fat1$^{LacZ/+}$* mice (Fig. 3A,B), endothelial cells (IB4+), have progressed through one-third of the retinal radius (Paredes et al., 2018; Stefater et al., 2011), whereas PAX2-expressing (PAX2+) astrocyte progenitor cells (APCs) have nearly reached the periphery (Tao and Zhang, 2014, 2016). Although β-galactosidase was detected throughout the *Fat1$^{LacZ/+}$* retina, it did not label growing vessels (IB4+), suggesting that, at this stage, *Fat1* expression occurs in the underlying neural retina, rather than in migrating ECs (Fig. 3B), confirming the adequacy of *Nestin-cre* for *Fat1* ablation.

Indeed, I detected a robust β-galactosidase signal on *Fat1$^{LacZ/+}$* retina sections, closely overlapping with GS signal, marking Müller glia in the neuroblast layer (NBL), where neurogenesis is still active
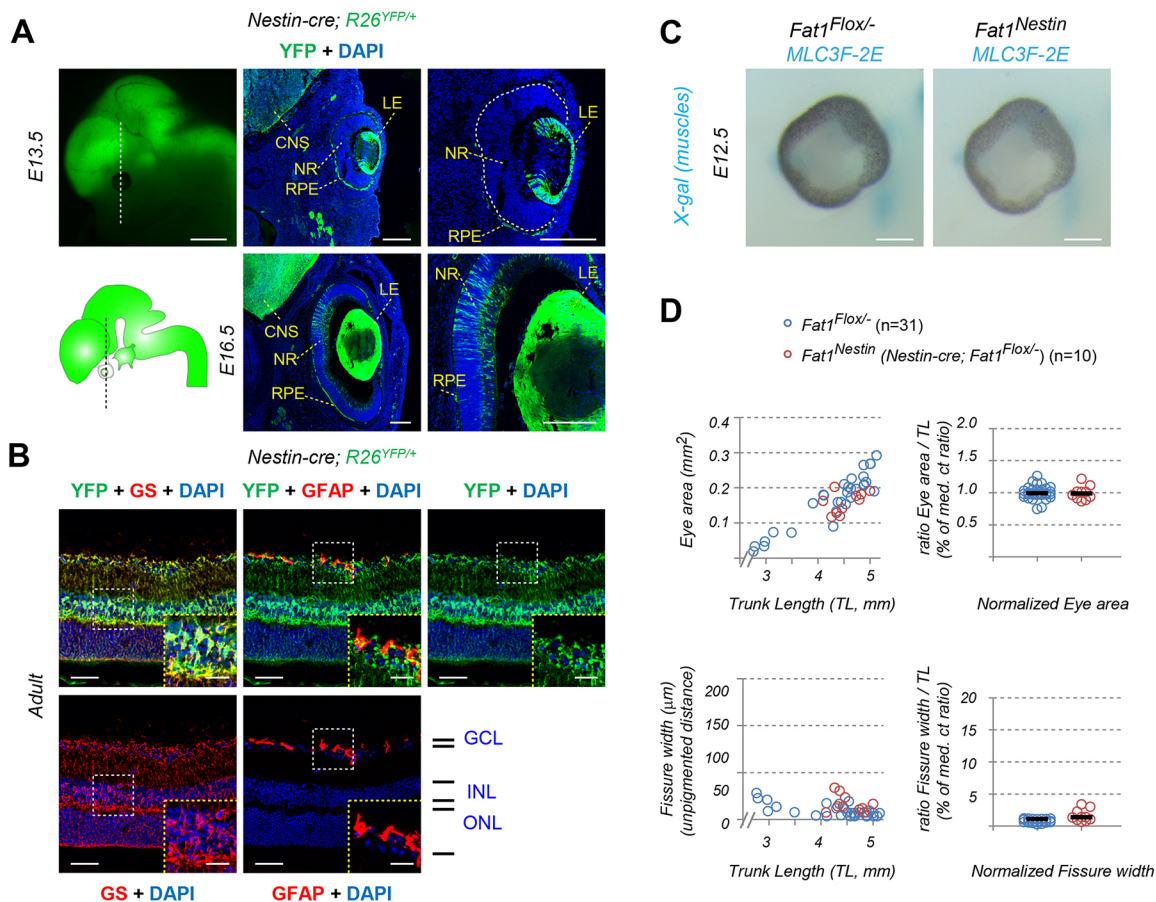
Fig. 2. Late *Nestin-cre*-driven recombination in the neural retina preserves eye morphogenesis. (A,B) *Nestin-cre* activity was evaluated by monitoring YFP expression in *Nestin-cre; R26^{YFP/+}* embryos (A, E13.5 and E16.5) or adult mice (B). (A) Top left, direct fluorescence; other panels, YFP (green) and DAPI (blue) staining on sections. The dashed vertical lines in A indicate the level of the sections. (B) In adult *Nestin-cre; R26^{YFP/+}* retina sections, YFP immunostaining (green) is combined with antibodies against glutamine synthetase (GS, red, left) or GFAP (red, middle). Insets show higher magnifications of regions outlined with by dotted lines. (C) Eye morphology was analyzed at E12.5 (top) and E13.5 (bottom) to compare *Nestin-cre; Fat1^{Flox/-}* (referred to as *Fat1^{Nestin}*) with control *Fat1^{Flox/-}* embryos (also with *MLC3F-2E* transgene). (D) Quantifications of ventral optic fissure width indicate that delayed *Fat1* deletion in neural tissue efficiently preserved eye morphogenesis. CNS, central nervous system; LE, lens epithelium; NR, neural retina; RPE, retinal pigmented epithelium; GCL, ganglion cell layer; INL, inner nuclear layer; ONL, outer nuclear layer. Scale bars: in A, 1 mm (top left); 200 μm (middle and right); in B, 50 μm and 20 μm (insets); in C, 200 μm.

(Fig. 3C, Fig. S1A,B). *Fat1^{LacZ}* expression was also prominent in the innermost layer, in cells with high levels of PDGFRα and GS (Fig. 3C) or GFAP (Fig. S1B), corresponding to astrocytes and APCs, as well as in scattered GS/PDGFRα/GFAP-negative cells, just underneath astrocytes, likely corresponding to RGC neurons (Fig. 3C, Fig. S1B). In contrast, low *Fat1* levels were detected in endothelial cells (CD31^{+}) and microglia (IBA1^{+}) (Fig. S1A).

Fat1 can be induced in vascular smooth muscle cells (VSMCs) in response to vascular injury to modulate the OXPHOS pathway (Cao et al., 2016), and cooperates with the transcriptional co-repressor atrophin to orient VSMC migration (Bruder-Nascimento et al., 2014; Hou et al., 2006; Hou and Sibinga, 2009). *Fat1* is also part of a gene expression signature that characterizes arterial endothelial cells (Aranguren et al., 2013). However, *Fat1^{LacZ}* expression in putative VSMCs decorating large vessels or in a pattern highlighting arteries at a higher level than veins, was detected only at the end of the period of horizontal growth (P7) and in P21 retinas (Fig. S1C). This expression in VSMCs and arterial ECs nevertheless arises too late to influence horizontal vascular growth. Consequently, in the postnatal retina, astrocytes represent the likeliest site where *Fat1* expression might be relevant for EC migration.

Neural Fat1 ablation transiently delays vascular progression in the postnatal retina

To investigate whether neural *Fat1* activity was required for postnatal angiogenesis, I first analyzed vascular progression (Fig. 4). In *Fat1^{Nestin}* retinas, non-mutant ECs progress in a *Fat1*-deleted neural territory. The extent of vascular progression was monitored in P3 and P7 retinas stained with CD31 or GS-IB4 by assessing the distance between center and front of vascular progression (EC front), relative to the retinal radius. In control P3 *Fat1^{Flox/-}* mice, the EC front had progressed to ~50% of the retinal radius, whereas *Fat1^{Nestin}* mice exhibited a marked delay in vascular growth (median progression of 38%, representing 80% of the control progression) (Fig. 4A,C, left plot). At P7, the EC front had reached ~80% of the vascular radius in control mice, versus 73% in *Fat1^{Nestin}* retinas, resulting in a modest but significant shortening of the vascular coverage (~95% of the control progression) (Fig. 4B,C, right). A delay was also observed in *Fat1^{-/-}* retinas, even when considering only areas devoid of coloboma-associated morphological abnormalities (Fig. S2A,C). Together, these data show that neural-specific *Fat1* deletion transiently delays vascular progression, suggesting that neural *Fat1* activity non-cell-autonomously influences the speed/rate of EC migration.
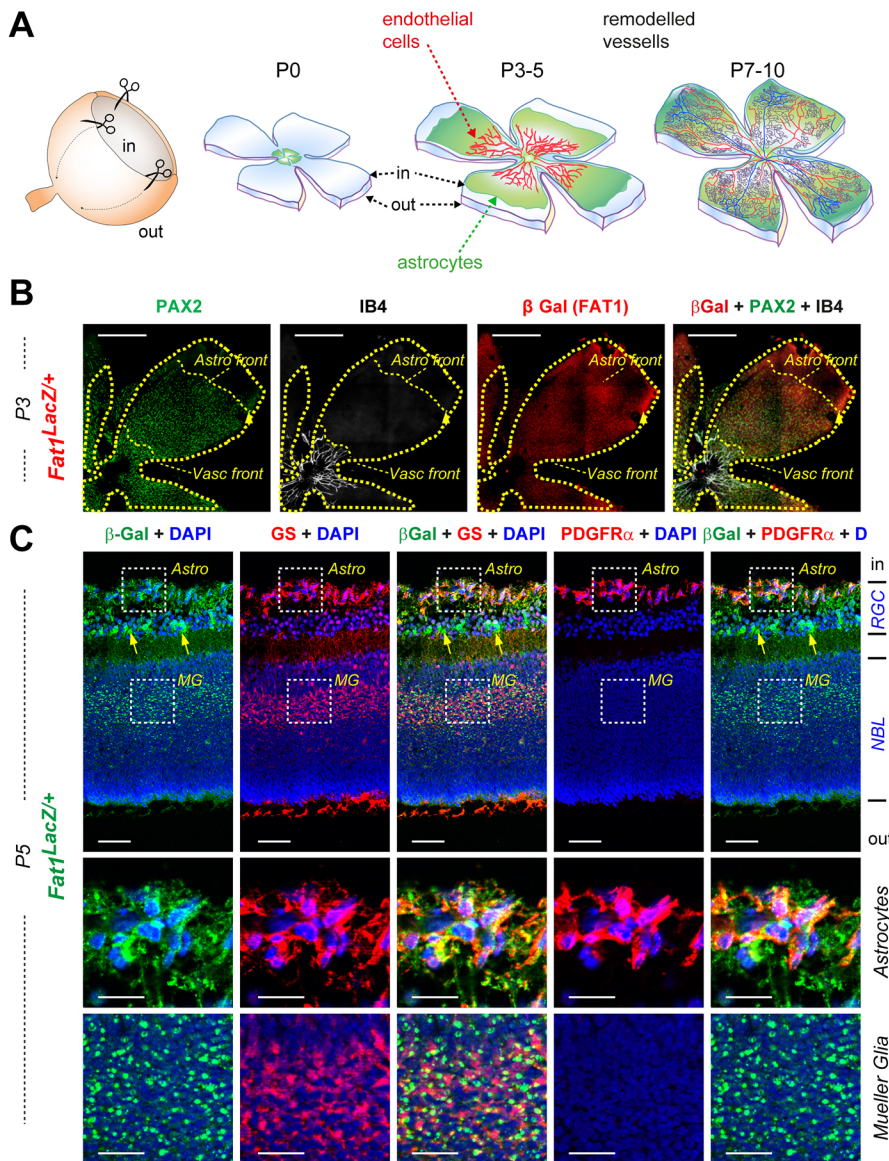
DEVELOPMENT

4

Fig. 3. *Fat1* expression in the postnatal retina.
(A) Schematic diagrams representing the method for opening and flat-mounting retinas, and progression of astrocytes and endothelial cells on flat-mounted retinas between P0 and P10. (B,C) *Fat1* expression was detected at P3 and P5 by following *Fat1^{LacZ}* expression in whole-mount retinas (B) or cryosections (C) using anti-β-galactosidase immunohistochemistry (red, B; green, C), combined with PAX2 (green, B), GS-IB4 (white, B), glutamine synthetase (GS, red, C), PDGFRα (red, C) and DAPI. Middle and bottom rows in C show higher magnification of regions outlined with dotted lines, focusing on the astrocyte layer (middle row) and neuroblast layer (NBL), where cell bodies of Müller glia (MG) are found. Scale bars: 500 µm in B; in C, 50 µm (top row); 20 µm (higher magnification images).

Neural-specific Fat1 ablation persistently impacts adult retinal vascular architecture

Although the effect of neural *Fat1* ablation on postnatal vascular growth was transient, it was associated with persistent abnormalities of the vascular architecture in adult retinas, visualized by immunolabeling with endothelial markers [CD31 (Fig. 5), GS-IB4 and claudin5 (Fig. S3)]. The adult retinal vascular network is organized in three layers, intercalated with neuronal layers (Fig. 5B-D). Large vessels (arteries and veins) radiate through the inner layer, from center to periphery, sharing space and direction with RGC axons, forming the nerve fiber layer (NFL) (Ruhrberg and Bautch, 2013). The NFL comprises veins, arteries and their ramifications. The first-order branches further ramify into smaller branches, with diameter decreasing with hierarchical level, and reach deeper layers via vertical branches (Fig. 5C,D). At two distinct levels – corresponding to interfaces between inner and outer nuclear layers (INL and ONL) and between ONL and rods/cones layer (Fig. 5C) – these vessels make 90° turns, and establish honeycomb-like horizontal vascular networks composed of capillaries, called inner and outer plexiform layers (IPL and OPL, Fig. 5C,D). I acquired images of fluorescent labeling throughout the depth of

flat-mounted retinas, and extracted (for a same position) images corresponding to each layer (Fig. 5B,D; yellow-dotted square in Fig. 5A), each of which was assigned a specific virtual color, to reconstitute the whole vasculature in a merged image (Fig. 5B, bottom row).

Although the overall appearance of retinal vasculature was preserved in *Fat1^{Nestin}* retinas (Fig. 5A), I nevertheless detected changes in the layered organization (schematized in Fig. 5E). For each layer, I measured vessel density, cumulated vascular length (see Materials and Methods) and number/complexity of junctions between horizontal and/or vertical branches (Fig. 5F). Compared with controls, *Fat1^{Nestin}* retinas exhibited an increased vascular density, length and number of intersections in the OPL (Fig. 5E), and an increased branching complexity (more junctions associating multiple segments) (Fig. 5G). This was associated with a change in the distribution of veins and arteries. In control retinas, veins form by convergence of collecting vessels towards the edge of the retina, where they coalesce into larger veins, fusing (arrowhead, Fig. 5A,B) to form one large vein, running in the NFL towards the retinal center. In contrast, I frequently observed that only the proximal regions of large veins were located in the NFL in *Fat1^{Nestin}* retinas (starting
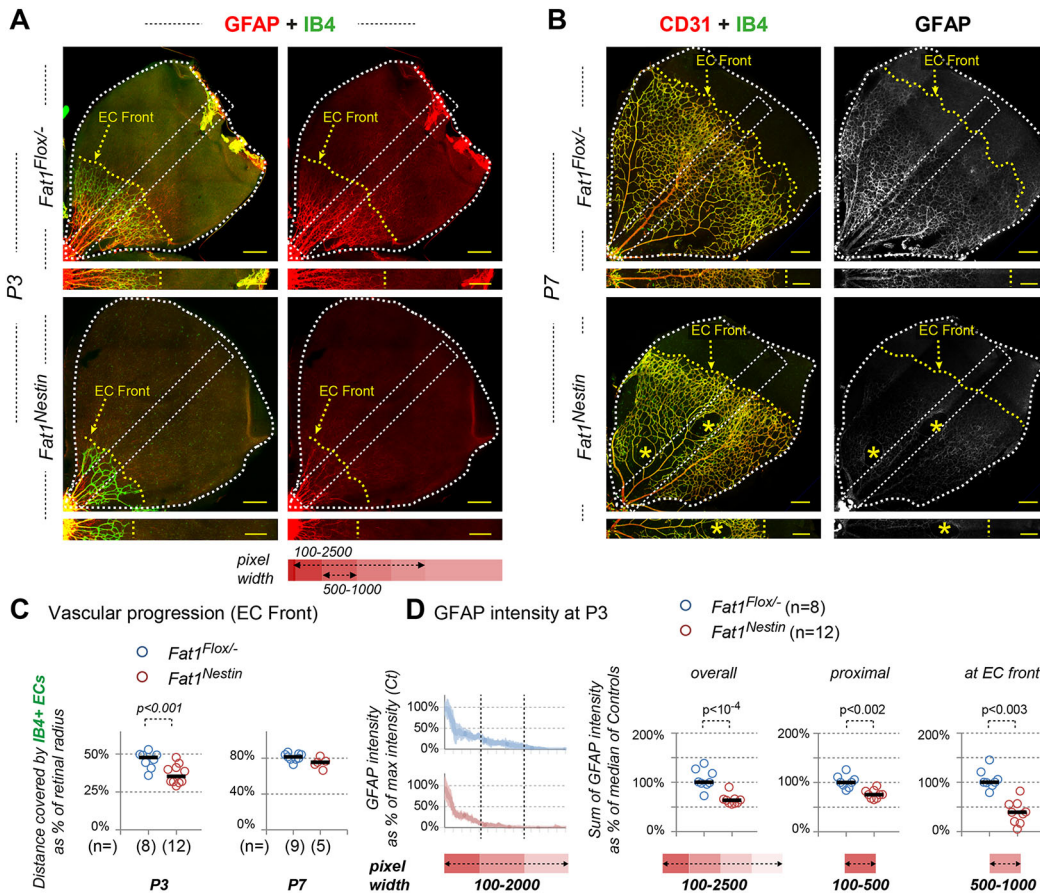
Fig. 4. Neural *Fat1* ablation delays endothelial cell progression through the postnatal retina. Flat-mounted retinas from *Fat1^Flox/−^* and *Fat1^Nestin^* mice at P3 (A) and P7 (B), after immunohistochemistry with GS-IB4 lectin (green) and antibodies against GFAP (red, A; white, B) or CD31 (red, B). Lower pictures in A and B correspond to outlined areas extending from center to periphery in retina quadrants, in which quantifications in C and D were carried out. (C) The distance covered by IB4-positive ECs was measured along the center-periphery axis, and expressed as percentage of retinal radius. Asterisks in B indicate patches devoid of ECs and astrocytes. (D) GFAP staining intensity was quantified along retinal radius (in outlined areas). Left plots: average intensity distribution along the radius for each genotype. Right plots: sum of signal intensity for window spanning the distances covering: the full width (100-2500), a small proximal window (100-500) or a window matching the shifting EC front (500-1000) (pixel coordinates are defined on the colored scale below the images in A). For each scatter plot, dots represent individual mice (with *n* indicated for each genotype); the thick central black lines mark median values and *P*-values were calculated using the parametric Mann-Whitney *U*-test. Scale bars: 200 µm.

from a discrete point found in random position along the retinal radius; arrows, Fig. 5A,B; arrowheads, Fig. S3A,B). Such a transition point corresponds to the position where a collecting vessel shifts from the OPL to the NFL (Fig. 5A,B,E, arrows), and is marked in *Fat1^Nestin^* retinas by gaps in the astrocyte coverage (Fig. S3A, asterisk). Overall, *Fat1* ablation in the neural lineage influences vascular remodeling by favoring the emergence of large collecting vessels in deep layers, with an increased vascular density.

These changes were accompanied by the appearance in the OPL of *Fat1^Nestin^* retinas of capillary segments decorated with vascular smooth muscle cells (VSMCs), identified by expression of smooth muscle actin α (αSMA, product of *Acta2*), a feature that was only observed in large vessels and first order ramifications in control retinas (Fig. S3C,D). Ectopic VSMC recruitment occurred in areas of *Fat1^Nestin^* OPL with typical capillary plexus morphology, whereas these capillaries are devoid of αSMA^+^ cells in control retinas. Finally, in two out of five *Fat1^Nestin^* mutant retinas, I also observed an increased expression of PLVAP (Fig. S3C), an adhesion molecule associated with endothelial fenestrations that must be silenced in CNS vessels to ensure blood brain barrier integrity (Shue et al., 2008; Stan et al., 2004). This increase, however, was not associated with a lowering of the tight junction

protein CLDN5 (Fig. S3C-E), also considered key for endothelial barrier function. Given that endothelial cells and VSMCs do not derive from the *Nestin-cre* lineage, all these phenotypes represent non-cell autonomous consequences of *Fat1* ablation in the neural lineage. This implies that ablation of *Fat1* activity in the neural lineage (including astrocytes, Müller glia, and neurons) has long-term effects on vascular architecture.

Neural Fat1 ablation alters the astrocyte coverage of the postnatal retina

Having confirmed that *Fat1* ablation in the neural lineage non-cell autonomously interferes with postnatal angiogenesis and causes persistent vascular abnormalities in adults, I next attempted to further characterize the postnatal vascular phenotype observed at P3-P7. I first asked whether this vascular phenotype was associated with phenotypes affecting *Nestin-cre*-derived cells involved in angiogenesis. Among those, astrocytes and their progenitors play an active role driving endothelial cell migration (Selvam et al., 2018; West et al., 2005), and expressed robust *Fat1* expression (Fig. 3B), prompting me to evaluate the impact of neural *Fat1* deletion on astrocyte distribution or maturation, first with the astrocyte marker GFAP.
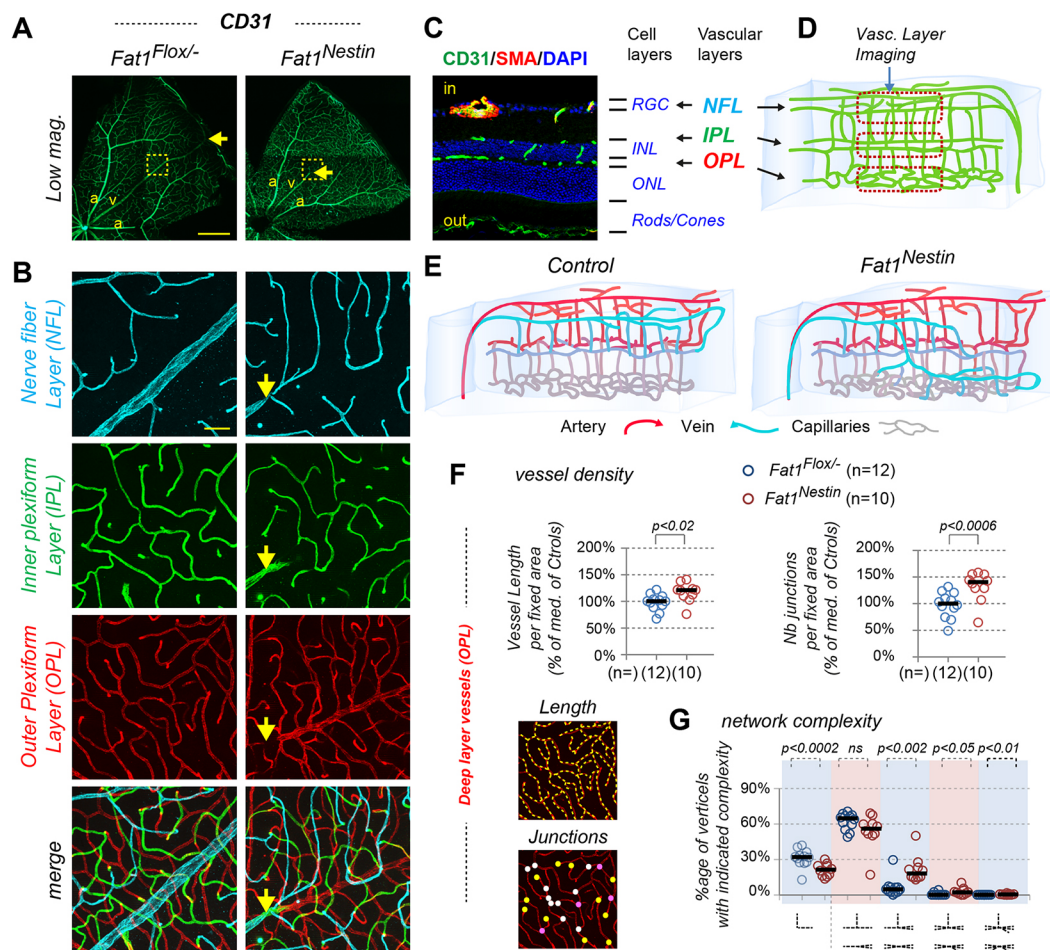
Fig. 5. Adult mice with neural Fat1 ablation exhibit persistent vascular phenotypes. (A,B) Flat-mounted adult retinas from $Fat1^{Flox/-}$ and $Fat1^{Nestin}$ mice, immunostained with CD31 antibodies. a, arteries; v, veins. (A) Low magnification; (B) high magnification images of the three vascular layers in the outlined regions in A, with colors corresponding to maximal intensity projections (MIP) of optical stacks schematized in C: nerve fiber layer (NFL, blue); inner plexiform layer (IPL, green; outer plexiform layer (OPL, red). Arrows in A and B indicate the transition point where a collecting vessel shifts from OPL to NFL. (C) Section of an adult wild-type retina immunostained with CD31 (green), αSMA (Acta2, red) and DAPI, illustrating vascular and nuclear layers. (D) Schematic representation of the retinal vascular organization showing corresponding depth of vascular layers shown in B. (E) Schematic representation of vessel type distribution (arteries/arterioles, red; veins/venules, blue; capillaries, gray) in control (left) and in $Fat1^{Nestin}$ (right) retinas. (F,G) Quantitative morphometric analyses: (F) total vessel length (left plot), number of junctions (right plot) per defined areas; one dot/mouse. (G) Vascular network complexity. The plot represents (for each genotype, one dot/mouse) the percentage of intersections with each complexity range, as represented schematically on the left. For scatter plots, dots represent individual mice (with $n=12$ for controls, $n=10$ for $Fat1^{Nestin}$), thick central black lines mark median values and P-values were calculated as follows: (F) using the parametric Mann-Whitney U-test; (G) using unpaired two-sided Student's t-test, assuming unequal variance. Scale bars: 500 μm in A; 50 μm in B.

GFAP intensity (low in the EC-free distal region, high in the vascularized region) reflects the switch of astrocytes from an immature/proliferative to a mature phenotype (Rattner et al., 2019; Tao and Zhang, 2014; West et al., 2005) (Fig. 4). The sharp transition in GFAP signal intensity coincides with the EC front (Fig. 4A,B, dotted line). As expected, the position of the $GFAP_{high}/GFAP_{low}$ transition in $Fat1^{Nestin}$ retinas matched the degree of vascular progression, reproducing the delay when compared with controls observed with EC markers: robust at P3 and milder at P7 (Fig. 4A-C, Fig. S2A). In addition, even in the region covered by endothelial cells, GFAP intensity appeared lower in mutant retinas. Analysis of signal intensity (see Materials and Methods) uncovered a global lowering of GFAP levels when considering a window spanning from the retina center to the periphery (encompassing both vascularized and non-vascularized areas), not only at P3 (Fig. 4D, left plot), but also at P7 (Fig. S2D). A large part of this reduction is likely accounted for by the delay in EC migration, as the sharp increase in GFAP level at the EC transition is triggered by the

proximity of endothelial cells (Duan et al., 2017, 2014; West et al., 2005). However, a strong lowering in $Fat1^{Nestin}$ retinas compared with controls was also observed in a window proximal to the vascular front (in Fig. 4A,B, the EC front is outlined by a yellow dotted line; and windows are defined by a color scale), where all astrocytes are in contact with ECs, even in mutant contexts (Fig. 4D, middle plot, window 100-500).

While analyzing CD31/GFAP-stained retinas at P7, I consistently observed patches devoid of both endothelial cells and astrocytes in the rear of the EC migration front of $Fat1^{Nestin}$, or as large indentations in the EC front in $Fat1^{-/-}$ retinas (asterisks, Fig. 4B, Figs S2A and S4A). These patches appeared rounded, irrespective of their size and position, while the underlying retinal structure was preserved, as if they resulted from a rupture of the EC/astrocyte layer with detachment from the underlying layers, followed by tissue retraction. I next analyzed astrocyte coverage at higher resolution. The sharp boundary in GFAP level seen in control retinas (Fig. 4) corresponded, at higher resolution, to an increase in the density

of the GFAP[+] fibrillary meshwork between pre- and post-vascular areas (Fig. S4B). Furthermore the lowering in GFAP levels measured in *Fat1Nestin* retinas (Fig. S2D) was also observed at higher magnification (Fig. S4B), especially in the vascularized areas and at the level of the EC migration front. The meshwork of GFAP[+] fibrils delimits non-stained spaces, which appeared larger or more irregular in size in mutant retinas (Fig. S4B, distal/bottom row). The latter observations suggest the possibility that a defect in maturation might precede the oxygen/EC-induced transition.

Neural Fat1 ablation alters astrocyte migration and maturation

To further explore the possibility of early defects preceding astrocyte maturation, I next analyzed additional markers. Astrocytes and their progenitors can be recognized as expressing the transcription factor PAX2 (Duan et al., 2014; Tao and Zhang, 2014, 2016), whereas their maturation can be followed with GFAP or the PDGF receptor PDGFRA during the phase of migration. By highlighting nuclei of migrating APCs and immature astrocytes, PAX2 staining allows evaluating changes in cell numbers and density, and in the distance traveled through the retina (Fig. 6). Although there was a modest but significant shortening of the distance covered by PAX2^{+} APCs in mutant P3 retinas of *Fat1Nestin* mice compared with controls (Fig. 6E, left plot), indicating a reduced APC migration rate, the density of PAX2^{+} APCs was unaffected, even in proximal windows in the vascularized area (Fig. 6E). This indicates that the lowering in GFAP levels described above was a true effect of *Fat1* deletion on GFAP expression levels rather than a consequence of reduced astrocyte numbers. Thus, *Fat1* activity is required for astrocyte maturation even in the central-most astrocytes, after they underwent the EC-induced transition.

To further characterize how *Fat1* influences astrocyte maturation, I also examined expression of PDGFRα in P3 retinas (Fig. 6). PDGFA is a key RGC neuron-derived contributor that promotes migration of astrocyte progenitor cells expressing its receptor PDGFRα (Fruttiger et al., 1996; Gerhardt et al., 2003; Tao and Zhang, 2016). Similar to GFAP staining, PDGFRα levels are correlated with the progression of astrocyte maturation (Fig. 6A-C). However, the increase in PDGFRα expression is gradual, with a steady rise between distal APCs (lowest levels) and the EC front, whereas PDGFRα levels reach a plateau throughout the vascularized/proximal retina (Fig. 6A-C). Analysis of signal intensity across the retinal radius (Fig. 6C) confirmed the overall lowering of PDGFRα levels in *Fat1Nestin* retinas compared with controls (Fig. 6D, left plot). Plotting the sum of intensity in defined pre- or post-vascular windows (Fig. 6D) demonstrated a robust lowering of PDGFRα levels in middle and distal segments in *Fat1Nestin* compared with control retinas, resulting in a flattened slope in non-vascularized astrocytes (Fig. 6D). This contrasted with unaffected PDGFRα levels in the proximal region. Again, the reduction in PDGFRα levels in middle and distal segments occurred in areas where no significant change could be detected in the density of PAX2^{+} cells (Fig. 6E) (except in a subset of mutant retinas where the fixed 'distal' window coincided with the shifted position of the astrocyte front). Thus, the lowering in PDGFRα levels reflects a true effect on protein levels, hence a delayed astrocyte maturation.

Whereas the reduced astrocyte migration distance (Fig. 6E) is a possible consequence of lowered PDGFRα levels, reflecting the role of PDGFRα signaling on astrocyte migration, the lack of

change in the density of PAX2^{+} cells was somewhat unexpected, as PDGF signaling also regulates astrocyte progenitor proliferation (Fruttiger et al., 1996). This was nevertheless corroborated by the lack of change in the proliferation rate of APCs (percentage of Ki67^{+} APCs), observed both in windows at fixed positions (distal) or at positions defined by the migration front (tip) (Fig. 6F,G). Thus, there is a distinct sensitivity of astrocyte maturation, migration and proliferation to the changes in PDGFRα levels that result from neural *Fat1* ablation.

Fat1 activity modulates astrocyte migration polarity

Given the known role of FAT cadherins in modulating polarized migration events, the observed delay in astrocyte migration in *Fat1*-deficient retinas might also result from altered migration polarity. Near the migration front, the nuclei of PAX2^{+} astrocyte progenitors (where PDGFRα levels are the lowest) are elongated and exhibit a marked orientation preference in the radial direction (Fig. 7). PAX2^{+} nuclei of following astrocytes (with increasing PDGFRα levels) are aligned along the cellular connections highlighted by PDGFRα staining (Fig. 6B). I therefore analyzed the orientation of nuclei of PAX2^{+} APCs, by measuring the angle between the longest nuclear dimension and the radius. By convention, I attribute a 0° angle to the radial direction and a ±90° angle to the tangential direction. I measured APC orientation in the distal-most segment (migration front) and computed the percentage of nuclei in defined angle ranges (Fig. 7C). Whereas the most represented angles in control mice were within the ±0-10° range of angles with the outward radial direction, neural-*Fat1* ablation led to a marked change in angle distribution, with a lower proportion of nuclei aligned with the radial direction, and increased proportion in the ±30-90° range (Fig. 7C). Together, these results indicate that *Fat1* deletion interferes with orientation of migrating astrocyte progenitors at the leading edge.

Identifying cell types in which Fat1 activity acts to influence astrocyte migration

I next sought to elucidate possible ways by which *Fat1* modulates astrocyte progenitor migration and maturation, and to distinguish the respective contributions of its activities in several cellular players known to influence astrocyte migration and maturation. These include astrocytes, Müller glia or neurons, each of these cell types being equally targeted by the *Nestin-cre* driver (Fig. 2B). I first asked whether *Fat1Nestin* retinas exhibited signs of alterations in Müller glia or neurons that could contribute to the observed phenotypes. The delayed astrocyte migration and 'avascular' patches are reminiscent of phenotypes associated with altered integrity of the ILM, resulting from mutations in ECM genes or from their altered production by Müller glia (Gnanaguru et al., 2013; Tao and Zhang, 2016). However, I failed to detect any ILM abnormality, as illustrated by the smooth appearance of laminin-immunostained ILM on whole-mounted retinas (where anti-laminin antibody also highlights blood vessels) (Fig. S5A,B). Thus, *Fat1* is dispensable for ILM production, excluding a crucial contribution of Müller glia to the phenotypes of *Fat1Nestin* retinas. Although the preferential direction of astrocyte migration is also instructed by radially oriented RGC axons (O'Sullivan et al., 2017), I failed to detect any major alteration of the radial orientation of RGC axons (Fig. S5A,B). Nevertheless, labeling of RGC axons with an anti-acetylated tubulin antibody unexpectedly uncovered reduced levels of tubulin acetylation in *Fat1Nestin* retinas (Fig. S5C,D). Thus, although I cannot exclude the possibility that altered neuronal signaling cascades affect axonal microtubules, these data exclude
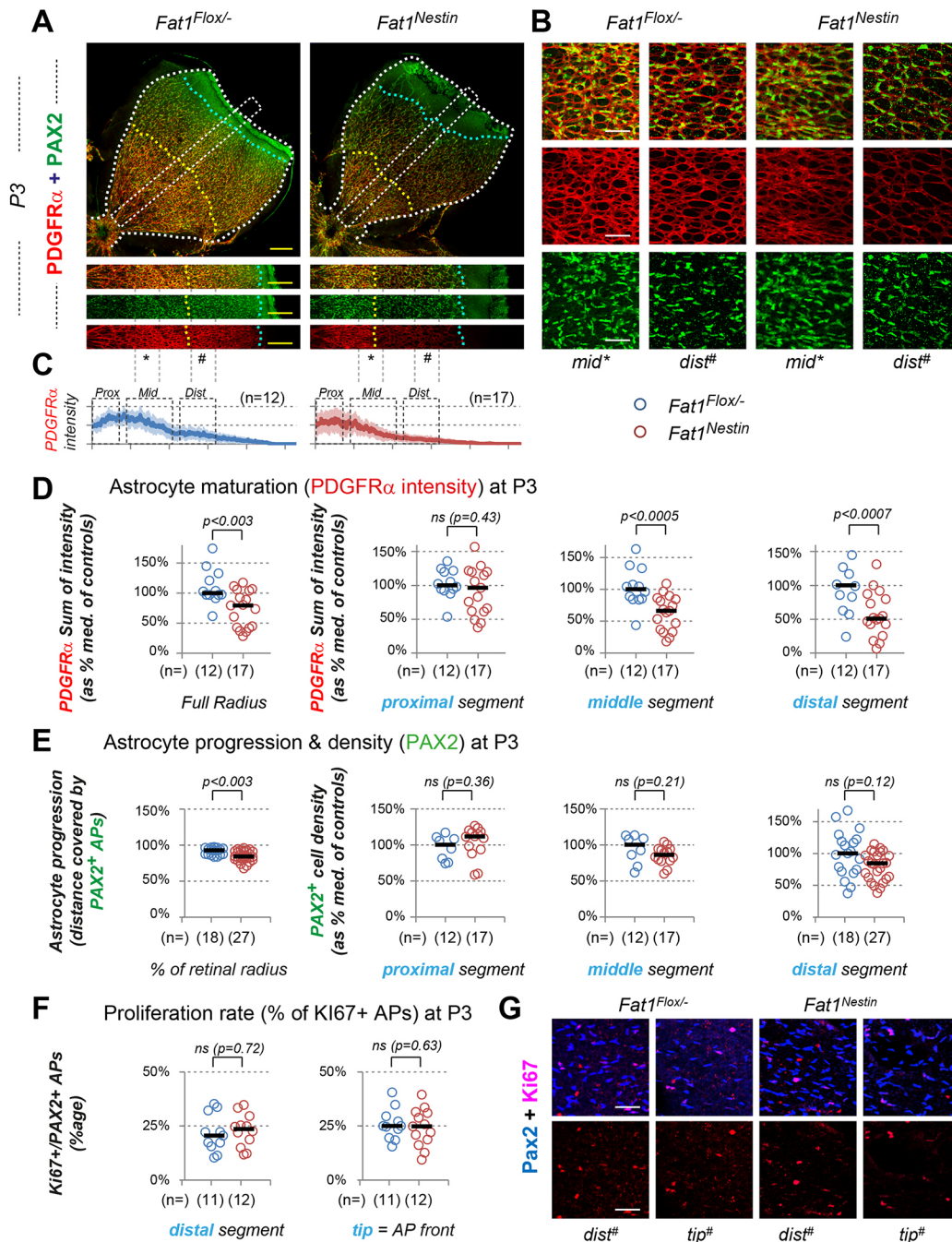
Fig. 6. Neural *Fat1* ablation interferes with astrocyte progenitor migration and maturation, but not proliferation. Flat-mounted P3 *Fat1*$^{Flox/−}$ and *Fat1*^{Nestin} retinas were stained with (A,B) PDGFRα (red) and PAX2 (green) or (G) PAX2 (blue) and Ki67 (red) antibodies. (A) Upper panels, retina quadrant; lower panels, bands extending from retinal center to periphery (dotted boxes) where quantifications were carried out. (B,G) High-magnification images matching middle (*) and distal (#) positions. The 'distal' area was positioned behind the shortest astrocyte span. (C) PDGFRα signal intensity was measured along the center-periphery axis [error bars indicate s.d. (lighter colors)]. (D) Sum of PDGFRα intensities (percentage of control median) for the full radius (left) or for indicated windows (right). (E) Astrocyte progression (distance reached by leading PAX2$^+$ astrocytes, left plot) and density (number of PAX2$^+$ cells/area, in indicated windows). (F) Proliferation (percentage of Ki-67$^+$ astrocytes) in the distal window, and in a window matching the AP front (tip). For scatter plots, dots represent individual mice (numbers indicated below each dataset), thick central black lines mark median values and *P*-values were calculated using the parametric Mann-Whitney *U*-test (D, prox, mid and dist) or an unpaired two-sided Student's *t*-test, assuming unequal variance (D, full radius; E,F). Scale bars: 200 μm in A; 50 μm in B.

axonal guidance defects as the main driver of the astrocyte polarity defect.

Finally, to assess astrocyte contribution in a direct manner, I ablated *Fat1* activity with an inducible *Pdgfra*$^{CRE−ERT2}$ driver, a context predominantly targeting migrating astrocytes when a pulse of tamoxifen is applied at P0, before migration onset (Fig. 8, Figs S6 and S7). I analyzed the migratory phenotype of recombined *YFP+* astrocytes in P3 retinas from *Fat1*^{ctrol}; *Pdgfra*^{iCRE}; *R26*^{YFP} (abbreviated as *Ctrol*$^{iPDGFRA-YFP}$) and *Fat1*$^{Flox/Flox}$; *Pdgfra*^{iCRE}; *R26*^{YFP} (*Fat1*$^{iPDGFRA-YFP}$) mice. Whereas *Fat1* ablation had no effect on the total number or proportion (around 5%) of YFP$^+$ astrocytes or on the overall progression of non-recombined
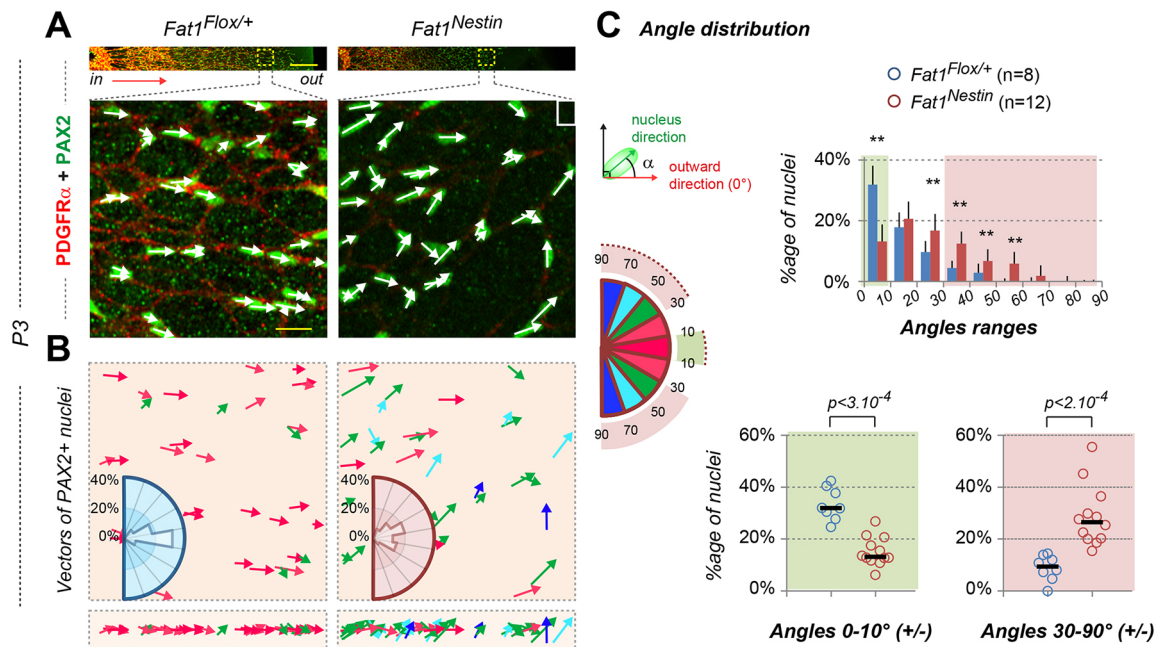
DEVELOPMENT

Fig. 7. *Fat1* controls the polarity of astrocyte progenitor migration. Imaging of astrocyte progenitor polarity in *Fat1*[Floxl−] and *Fat1*[Nestin] P3 retinas stained using PDGFRα (red) and PAX2 (green) antibodies, as in Fig. 6. (A) Upper pictures represent regions extending from retinal center to periphery. Lower pictures are higher magnifications of astrocyte progenitor cells near the migration front, with a white arrow highlighting each PAX2^{+} cell nucleus to visualize directional vector (nucleus length). (B) For each image, the same vectors were color coded as defined on the color-rose plot (right). For each genotype, a polar plot shows the average angle distribution of PAX2^{+} vectors representative of *Fat1*[Floxl−] (*n*=8) and *Fat1*[Nestin] (*n*=12) mice, measuring ~80-100 cells per mouse at the migration front (where PDGFRα expression level is the lowest). (C) Top: angle distribution of PAX2^{+} vectors (error bars indicate s.d.). Bottom: scatter plots (with one dot/ mouse) showing the proportion of PAX2^{+} astrocytes with angles in the 0-10° (left) and 30-90° (right) ranges. Statistics (parametric Mann-Whitney *U*-test): **$P<0.001$. Scale bars in A: 200 μm (top); 20 μm (bottom).

astrocytes, the proportion of *YFP*^{+} cells reaching the periphery at P3 (last 20% of the retinal radius) was reduced, reflecting a cell-autonomous effect on the migration span (Fig. 8A,B, Fig. S7). This was associated with a change in the distribution of astrocyte directions similar to the phenotype of *Fat1*[Nestin] mutants (Fig. 8C,D), and surprisingly with an increased proliferation (proportion of Ki67^{+}/PAX2^{+} nuclei among YFP^{+} cells, Fig. 8E,F). Of note, *Fat1*-deficient astrocytes exhibited comparable PDGFRα levels to their non-recombined neighbors (Fig. 8C), indicating that PDGFRα regulation by *Fat1* is not an astrocyte-intrinsic function. These data suggest that astrocyte-intrinsic *Fat1* activity is required to control astrocyte migration polarity and to limit their proliferation. The absence of proliferation defect in *Fat1*[Nestin] retina implies that there was a compensatory effect likely driven by ablation of *Fat1* activity in another cell type.

DISCUSSION
In this study, I investigated how FAT1 cadherin modulates retinal vascular development and integrity. As *Fat1* is required for optic cup closure during development, I bypassed this early requirement by disrupting its activity in the late neural linage owing to late-onset of *Nestin-cre* activity in the retinal epithelium, thus preserving eye morphogenesis. This context uncovered that retinal *Fat1* is required for coordinated migration polarity and subsequent maturation of astrocyte progenitors in the postnatal retina. Alteration of both processes in *Fat1*[Nestin] mutants interferes with the astrocyte/EC cross-talk and delays postnatal angiogenesis,. Inducible *Fat1* deletion in postnatal astrocytes allowed distinguishing astrocyte-intrinsic versus astrocyte-extrinsic modalities. Altogether, this unveils the functional versatility of FAT1 signaling, ensuring robustness of this dynamic developmental process.

Control by FAT1 signaling of astrocyte migration and maturation
This study has uncovered a key role of FAT1 signaling in astrocyte migration and maturation. Given the tight coupling between astrocyte and EC migration (Duan et al., 2017, 2014; Rattner et al., 2019; West et al., 2005), the delay in endothelial cell migration, and the effect on astrocyte maturation in the vascularized retina are likely secondary consequences of the astrocytes phenotypes, as they can impact the reciprocal astrocyte/EC cross-talk. Delayed astrocyte progression can shift the position of the pro-angiogenic VEGF gradient, and the resulting delay in EC progression and oxygen perfusion can in turn delay subsequent astrocyte maturation. Thus, logically, only the earliest phenotypic changes occurring at the leading edge of astrocyte migration are expected to be direct consequences of *Fat1* deficiency. These include a lowering of PDGFRα protein levels (Fig. 5) and the loss of preferential astrocyte direction.

PDGFRα expression gradually increases in migrating astrocyte progenitors between the leading edge and the vascularized area. This PDGFRα gradient may tune astrocyte sensitivity and responsiveness to PDGF along the retinal radius. PDGF, which is produced by RGC neurons, is known to promote astrocyte migration and proliferation (Fruttiger et al., 1996). Inhibition of PDGFRα signaling in the postnatal retina, by infusion with function blocking antibodies (Fruttiger et al., 1996) or by *Pdgfra* ablation in the astrocyte lineage (Tao and Zhang, 2016), has been shown to block migration and proliferation of astrocyte progenitors, thus also slowing vascular progression (Fruttiger et al., 1996; Tao and Zhang, 2016). In contrast, overexpression of PDGFA in transgenic mice resulted in enhanced astrocyte proliferation and density, while also blocking their migration (Fruttiger et al., 1996). Neural *Fat1* ablation resulted in lowered PDGFRα levels in astrocytes distal to
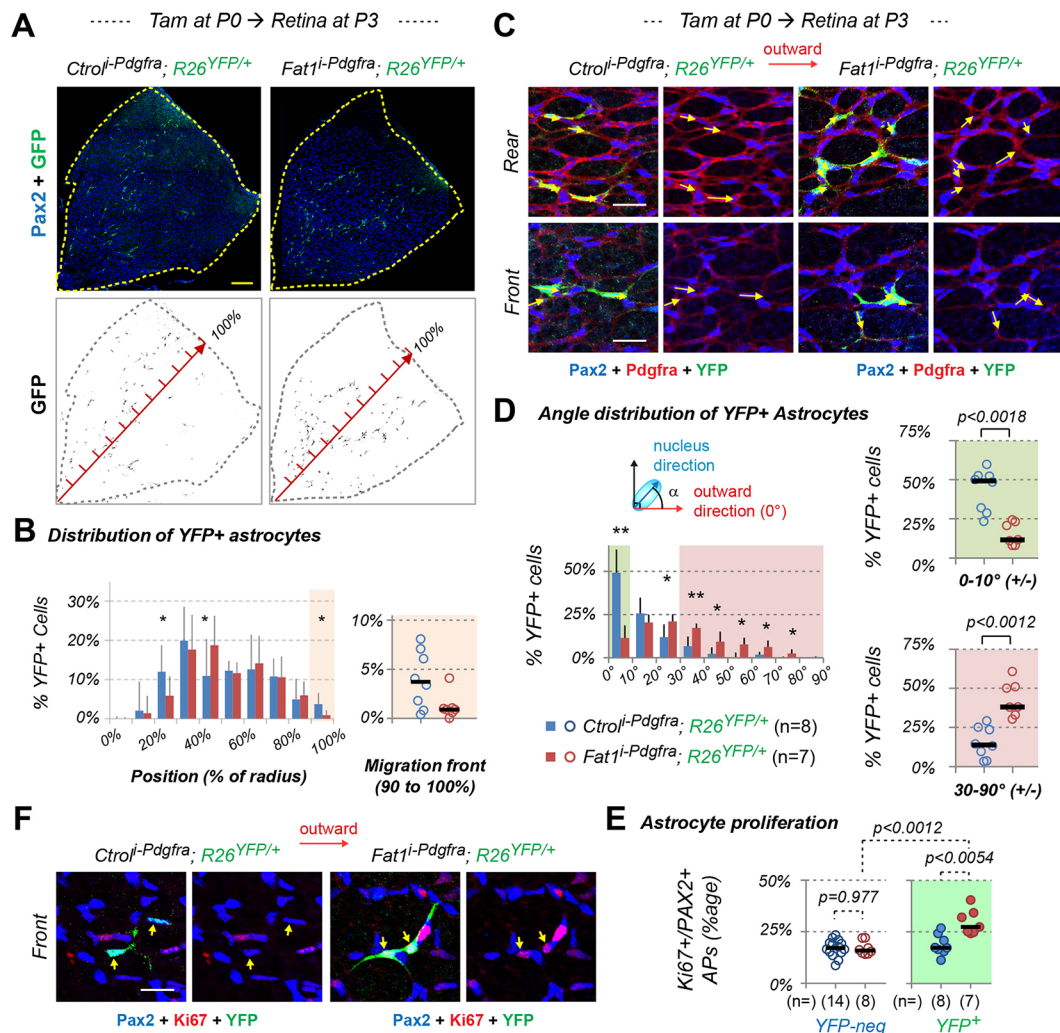
Fig. 8. Fat1 is required in astrocytes to modulate their directional migration and proliferation. (A,C,F) Flat-mounted P3 retinas from *Ctrl*[superscript]*Pdgfra-iCRE* and *Fat1*[superscript]*Pdgfra-iCRE* mice, which received tamoxifen at P0, stained using GFP (green), and PAX2 (blue), PDGFRa (red, C) or Ki67 (red, F) antibodies. (A) Overview of retina quadrants showing the distribution of YFP⁺ recombined cells. (C,F) High-magnification images showing representative examples of YFP⁺ cells near the migration front or in the rear (left, three colors; right, without YFP). (B) Analysis of YFP⁺ astrocyte distribution according to their position along the center-periphery radius (error bars indicate s.d.). Right plot features the last 10%. (D) Angle distribution of YFP⁺ cells. Left: distribution throughout all angle ranges (error bars indicate s.d.). Right: proportion of YFP⁺;PAX2⁺ astrocytes with angles in the 0-10° (left) and 30-90° (right) ranges. (E) Astrocyte proliferation (Ki-67⁺/PAX2⁺ percentage), for YFP⁻ and YFP⁺ cells. Bar graphs show median value for each genotype. Scatter plots provide data from individual mice; thick black lines mark median values [*Ctrl*[superscript]*Pdgfra-iCRE* (*n*=8), *Fat1*[superscript]*Pdgfra-iCRE* (*n*=7)]. *P*-values were calculated using a parametric Mann–Whitney *U*-test (D,E) or using an unpaired two-sided Student's *t*-test, assuming unequal variance (for bar plots). **P<0.001, *P<0.05. Scale bars: 200 µm in A; 50 µm in C,F.

the EC front. Unexpectedly, although astrocyte migration was impacted in *Fat1*[superscript]*Nestin* retinas, this phenotype was not associated with a reduction of astrocyte proliferation that would be expected from lowered PDGFRα signaling. Instead, *Pdgfra*[superscript]*iCRE*-driven astrocyte-specific inducible *Fat1* deletion at P0 led to an increase in astrocyte proliferation in recombined astrocytes, without any apparent change in PDGFRα level. This suggests a model in which *Fat1* activity in astrocytes negatively regulates their proliferation, as previously found in astrocyte and glioblastoma cell lines (Morris et al., 2013). As this astrocyte-intrinsic function does not impact PDGFRα expression (Fig. 8C), this suggests that the lowered PDGFRα levels observed in *Fat1*[superscript]*Nestin* retinas resulted from the suppression of *Fat1* activity in other cell types. According to this model, the two functions of *Fat1* (astrocyte-intrinsic and -extrinsic) would have antagonistic impact on proliferation, explaining the lack of proliferation phenotype in a context where both functions are deleted.

Astrocyte progenitors at the migration front exhibit a marked elongation of their nuclei in the direction of migration and are aligned along the retinal radius, and *Fat1* disruption resulted in a loss of this preferential orientation. The alignment of astrocytes along the outward radius is best seen at the migration front, where PDGFRα levels are the lowest, whereas in the rear, nuclei are aligned along PDGFRα⁺ cellular protrusions that are mainly oriented in the direction of migration. The change in polarity caused by *Fat1* deficiency is detected in these distal-most APCs. This polarity phenotype was reproduced by astrocyte-specific *Fat1* deletion induced at P0 by *Pdgfra*[superscript]*iCRE*, suggesting that control of orientation of migrating astrocytes by *Fat1* is an astrocyte-intrinsic function. The term astrocyte-intrinsic seems better suited than cell-autonomous in this case, because alignment of each cell along the outward direction may involve communication between *Fat1*-expressing astrocytes, possibly relying on bi-directional signaling by FAT1 and its partner(s). By uncoupling the effects of

Fat1-deletion on astrocyte orientation and on PDGFRα levels, this result suggests that the change in PDGFRα levels occurring in *Fat1^Nestin^* retinas was also not caused by altered polarity.

The preferential direction of astrocyte migration has been reported to be instructed by radially oriented RGC axons (O'Sullivan et al., 2017). Although I uncovered a significant deficit in tubulin acetylation, a post-translational modification influencing microtubules rigidity that has the potential to influence axonal morphology, growth and function (Morley et al., 2016; Moutin et al., 2021), *Fat1*-deficient RGCs did not exhibit any axonal orientation abnormalities. Whereas altered astrocyte polarity is unlikely to result from axon guidance defects, I cannot exclude the possibility that alterations in axonal microtubule dynamics could have a subtle effect on the dynamics of astrocyte migration and maturation.

Impact on vascular pathologies

Retinal vascular pathologies are becoming a major medical challenge, with the widespread occurrence of age-related macular degeneration, diabetic retinopathies or stroke (Quaegebeur et al., 2011). The present study identifies *Fat1* as a novel modulator of astrocyte maturation, the deletion of which in neural lineages impacts on the astrocyte/endothelial cell coupling, thus delaying postnatal angiogenesis, and causing persistent vascular phenotypes in adult retinas. I have not yet distinguished whether these adult phenotypes represent late consequences of the early abnormalities or whether they highlight additional roles of *Fat1* during adult vasculature homeostasis. The increased vascular density and the presence of large collecting vessels in deep layers of *Fat1^Nestin^* retinas are consistent with the possibility of neovascularization events such as those occurring after transient ischemic events or vessel ruptures, owing to the capacity of hypoxia to induce VEGF expression. Although, so far, none of the genome-wide association studies has identified *FAT1* mutations as being causally involved in any of the known human retinal pathologies, genetic and/or regulatory *FAT1* alterations have been associated with facioscapulohumeral muscular dystrophy, a neuromuscular pathology frequently associated with retinal vascular symptoms (Caruso et al., 2013; Mariot et al., 2015; Puppo et al., 2015). The present results, by linking *Fat1* dysfunction to defective neurovascular communication, emphasize the key roles of astrocytes and uncover *Fat1* signaling as a new component in the cellular cross-talk ensuring robustness of retinal vascular development.

MATERIALS AND METHODS
Mice

Animals were maintained and sacrificed in accordance with institutional guidelines. All procedures involving the use of animals were performed in accordance with the European Community Council Directive of 22 September 2010 on the protection of animals used for experimental purposes (2010/63/UE). The experimental protocols were carried out in compliance with institutional Ethics Committee guidelines for animal Research (comité d'éthique pour l'expérimentation animale – Comité d'éthique de Marseille) and in compliance with French law, under an agreement (D13-055-21) delivered by the Préfecture de la Région Provence-Alpes-Côte-d'Azur et des Bouches-du-Rhône. Mice were sacrificed at P3, P5 or P7 for postnatal studies. For collection of adult samples, mice were anesthetized with lethal doses of ketamine and xylasine, and euthanized by transcardiac perfusion with 4% PFA.

The mouse lines used in this study are maintained in a B6D2 background, by performing regular back-crosses with commercial B6D2-F1J/RJ mice. Table S1 provides the Mouse Genome Informatics (MGI) reference number

and link to the information page, a brief description of how it was made and a reference to the article describing their production. These include three mutant alleles of the *Fat1* gene, all described and characterized in previous studies (Caruso et al., 2013; Helmbacher, 2018): (1) a *Fat1^LacZ^* genetrap allele [*Fat1^Gt(KST249)Byg^*; Leighton et al., 2001], in which *LacZ* expression reproduces that of the endogenous *Fat1* locus; (2) a *Fat1^Flox^* conditional allele (*Fat1^tm1.1Fhel^*), in which exons 24 and 25 (the latter containing the transmembrane domain) are flanked by LoxP sites; and (3) the constitutive knockout allele *Fat1⁻* (also known as *Fat1^ΔTM^* or *Fat1^tm1.2Fhel^*) derived from the *Fat1^Flox^* allele by permanent cre-mediated deletion. Tissue-specific ablation in the neural lineage was achieved either with the *Nestin-cre* line [Tg(Nes-cre)1Kln line; Tronche et al., 1999] or, in migrating astrocytes, with the inducible Pdgfra-CRE/ERT2 line (Rivers et al., 2008) (abbreviated *Pdgfra^iCRE^*). I used the *R26^YFP^* line [Gt(ROSA)26Sor^tm1(EYFP)^Cos line (Jackson laboratory mouse strain 006148); Srinivas et al., 2001] as a reporter of cre-mediated activity. Some of the embryos in which I study the coloboma phenotype also carry the transgenic line *MLC3F-2E-LacZ* [also known as Tg(Myl1-lacZ)1Ibdml; Kelly et al., 1995, 1997]. Genotyping was carried out as previously described for each line, except for the new genotyping oligonucleotides that allow specific detection of the *Nestin-cre* transgene (Nes-Fw: 5′ AAG GGT TAA GGC CTA GGG ACC GCC C 3′) or of the *Pdgfra^iCRE^* allele (Pdgfra-Fw: 5′ GCC CAC CAG TGG CTT TCT GTT TGG C 3′), each of which combined with a reverse primer in the CRE sequence (Cre-Rev: 5′ TTC AGG TTC TGC GGG AAA CCA TTT CC 3′).

As recently mentioned in a survey of various cre-lines (Luo et al., 2020), the *Nestin-cre* line exhibits a noteworthy amount of activity not only in the female germline (as previously described; Haigh et al., 2003), but also in the male germline. Thus, when the transgene is carried by the same individual as the Floxed allele, Cre activity in the male germline can lead to the transmission by males of a *Fat1⁻* recombined allele instead of the non-recombined allele (~50% in the present study). Presence or absence of the recombined allele was evaluated by PCR. The crosses meant to produce mutants and littermate controls involved a *Nestin-cre; Fat1^Flox/+^* or *Nestin-cre; Fat1^Flox/Flox^* male, mated with *Fat1^Flox/Flox^* females, which therefore represented a source of non-recombined allele. Thus, mutants derived from these crosses can be *Nestin-cre; Fat1^Flox/Flox^* or *Nestin-cre; Fat1^Flox/−^* (the two genotypes being pooled in my quantifications and collectively called *Fat1^Nestin^*), whereas controls can be *Fat1^Flox/Flox^*, *Fat1^Flox/−^* (the two genotypes being also pooled), even when they did not inherit the cre transgene. I also included some *Nestin-cre; Fat1^Flox/+^* or *Nestin-cre; Fat1^+/+^* controls in adult studies and obtained similar results.

Tamoxifen induction

For *Fat1* ablation in migrating retinal astrocyte progenitors at postnatal stages, I took advantage of their transient *Pdgfra* expression, and used the inducible *Pdgfra^iCRE^* line, combined with the *R26^YFP^* reporter and the conditional *Fat1* allele. The crosses intended to produce mutants and littermate controls involved *Fat1^Flox/Flox^; Pdgfra^iCRE^; R26^YFP/YFP^* or *Fat1^Flox/+^; Pdgfra^iCRE^; R26^YFP/YFP^* males mated with *Fat1^Flox/Flox^* or *Fat1^Flox/+^* females. At P0, after pregnant females completed delivery, all pups of the litter were injected with ~10 μl of tamoxifen (10 mg/ml in corn oil), using BD 0.3 ml insulin syringes (30G). Analyses were carried out by following YFP⁺ cells in *Pdgfra-icre; R26^YFP/+^* pups, with the control group (*Ctrol^iPDGFRA-YFP^*), including *Pdgfra-icre; R26^YFP/+^; Fat1^+/+^* and *Pdgfra-icre; Fat1^Flox/+^; R26^YFP/+^* mice, compared with the mutant group (*Fat1^iPDGFRA-YFP^*) consisting of *Pdgfra-icre; R26^YFP/+^; Fat1^Flox/Flox^* pups.

Tissue collection and immunohistochemistry

Embryos were collected in ice-cold PBS and fixed in 4% paraformaldehyde (PFA) in phosphate-buffered saline (PBS) for 3-5 h. Retinas from neonate mice were dissected from freshly dissected eyes previously immersed for ~1 h in 4% PFA, and were post-fixed for a maximum of 2 h. Hyaloid vessels were manually removed from P3-P7 retinas prior to post-fixation (to avoid tissue damage and consequent artifacts). Retinas from adult mice were dissected after transcardiac perfusion with fresh 4% PFA, and also post-fixed for 1-2 h. All tissues/embryos were then rinsed in PBS, and were either used directly for whole-mount immunohistochemistry (IHC) (free-floating

retinas) or cryoprotected, embedded and frozen for cryostat sectioning to perform immunohistochemistry on sections.

In the case of preparations for cryosections, tissues were cryo-protected by overnight immersion in 25% sucrose in PBS at 4°C, and embedded in a mix of 7.5% gelatin and 15% sucrose (maintained liquid in a 42°C bath and solidified on ice after adding the tissue). Once solidified, the position/ orientation of the sample was indicated with a marker, prior to freezing the sample in isopentane and kept cold in a carbo-ethanol bath (dry ice/ethanol). Frozen samples were cryosectionned with a Zeiss cryostat (10 μm) and sections were kept at −20°C until use.

For immunohistochemistry, cryostat sections or free-floating retinas were first incubated in PBS containing 0.3% Triton X-100 for permeabilization. They were then subjected to a bleaching step in 6% hydrogen peroxide (H_2O_2) (mixing one volume of 30% H_2O_2 with four volumes of PBS containing 0.3% Triton X-100) for 30 min. For some antibodies (listed in Table S2), a step of heat-induced epitope retrieval (HIER) of cryostat sections was carried out prior to antibody incubation, by incubation in HIER solution at 95°C for 5-10 min. The HIER solution [0.1 M citrate buffer (pH 6.0) and 0.2% Tween-20] was preheated until it started boiling. Sections, pre-stabilized in cold HIER solution, were placed in the boiling HIER solution for a fixed time. Sections or floating retinas were then rinsed again (three times) in PBS containing 0.3% Triton X-100, and incubated in a blocking solution containing: 20% newborn calf serum (NCS), PBS containing 0.3% Triton X-100, together with the desired antibodies. When performing staining with the isolectin IB4, 1 mM of $CaCl_2$ and 1 mM $MgCl_2$ were added to all solutions to allow efficient lectin binding.

Incubations with primary antibodies or lectin were carried out in blocking solution (with Ca/Mg) overnight at 4°C under agitation. All antibodies and binding reagents, references and conditions of use are listed in Table S2. Following incubation with primary antibodies, retinas were rinsed multiple times in PBS containing 0.3% Triton X-100 (at least five times for 15 min). Incubations with secondary antibodies were performed in blocking solution for 1 h 30 min at room temperature, under agitation (or overnight at 4°C), after which samples were rinsed again multiple times (minimum five times) in PBS containing 0.3% Triton X-100. After completing the immunostainings, retinas were flat mounted and covered with mounting medium containing Prolong Gold anti-fade reagent and DAPI (Table S2). Images were acquired on a Zeiss AxioImager Z1 equipped with Apotome.

Imaging and quantification methods

Measurements of the relative eye area and grove width were carried out on images of embryos acquired with a Leica stereomicroscope and exploited using Axiovision software, following the procedure described previously (Helmbacher, 2018). The wild-type and $Fat1^{-/-}$ embryos were the same sample set as those in which muscle development was previously analyzed, thus sharing trunk length normalizing values (Helmbacher, 2018).

Quantifications of signal intensities (GFAP, PDGFRα and acetylated tubulin) were carried out using an approach similar to the method my colleagues and I previously described for quantifying *in situ* hybridization signal (Fan et al., 2015; Helmbacher, 2018). 10x mosaic images of flat-mounted retinas encompassing a quadrant were acquired, using an identical exposure time for all analyzed samples (e.g. 290 ms for PDGFRα intensity analysis). Images were rotated, such that a region of interest (ROI), encompassing a radius from the retina center to the periphery, is positioned horizontally, with the center to the left. A fixed size ROI (300×3000 pixels, representing 200×2000 μm) was cropped, positioning its left border at the inner extremity of the optic stalk. Signal intensity along the entire ROI was then analyzed using ImageJ (analyze>plot profile) and data were exported for statistical analysis. Raw values (intensity ranging from 0 to 250) were then processed as described (Fan et al., 2015; Helmbacher, 2018). Because all ROIs included a peripheral region with minimal astrocyte coverage, this was used to define a fixed window (coordinates 2500-3000) for baseline intensity measurement (the baseline being the median value in the window, representing the background intensity). The window was manually adjusted in the case of an obvious artefact (damaged or folded retinal border). A median baseline was calculated for all controls of a same experimental series, and this value was subtracted from intensity measurement of each sample. The resulting intensity was thresholded at 0 (to avoid negative

values). The maximal value was measured for each sample, in a window excluding the central ring (the thickness/intensity of which depended on the dissection). The maximal amplitude was calculated by subtracting the baseline from the maximal value. A median maximal amplitude (MMA) was calculated for controls (MMAc) in each experimental group, and used for normalizing all data. The intensity was thus expressed as percentage of the MMAc (by dividing the thresholded intensity by the MMAc; 100% corresponded to the MMAc), which varied along the proximo-distal coordinates of the ROI. For each mouse, the sum of intensity (area under the curve) was then calculated, either for the full radius (pixels 350-3000, excluding the inner ring) or for windows of fixed width (pixels 350-700; 800-1400 and 1500-2000 for PDGFRα; pixels 100-500; 500-1000 and 1000-1500 for GFAP; and pixels 1500-1800 for acetylated tubulin).

For the angle distribution analysis, a set of ~100 PAX2^{+} nuclei was analyzed per mouse at the migration front in the same ROI (from the retina center to the periphery, 300×3000 pixels) from mosaic images of whole retinas. For each mouse, I calculated the percentage of nuclei displaying an angle in each angle category [ranges (±) 0-10°, 10-20°, 20-30°, 30-40°, 40-50°, 50-60°, 60-70°, 70-80° and 80-80°, with 0° representing the main outward direction (radius), in the width of the considered ROI]. Thus, in each angle range, the analysis allowed retrieving one output value per mouse. Scatter plots showing each value are shown for the ±0-10° range and for a large angle group cumulating ±30-90°.

Analyses of the distribution of YFP[+] or PAX2^{+} cells were performed on images of flat-mounted retinas, including in a fixed-sized ROI for Fig. 8: an entire retinal quadrant, with the retinal center coinciding with a corner of the ROI (rotating images for the reference corner to be always bottom left). For Fig. S7, instead, the ROI was a band spanning from the center to the periphery. Images of the YFP signal (Fig. 8) or of PAX2^{+} cells were thresholded in ImageJ (image>threshold), using the same threshold (and exposure time) for all. Analyses of the respective distribution of YFP[ON]/ PAX2^{+} and YFP[OFF]/PAX2^{+} cells (Fig. S7) were carried out as depicted in Fig. 7B, by using color selection in the YFP[+] channel, to delete the corresponding subset of cells in the PAX2 channel, thus generating distinct images for the two cell subsets. Then, using the 'Analyze particles' function, a descriptor including its area and positions [length (X) and height (Y)] was obtained for each object. These results were exported in an .xls file for each sample. I first sorted objects by area, and selected all objects larger than a threshold size (to exclude staining artefacts or objects smaller than cell bodies). I then calculated the distance of each YFP[+] cell to the reference central position [square root of the sum of squared distances, when using corner in Fig. 8, or length (X), when using a band spanning the radius in Fig. S7] and divided this number by the calculated retinal radius (distance between retinal edge and reference center position). Thus, for each image, the position of each cell is expressed as a percentage of the retinal radius. This allowed the distribution (percentage of cells in each 10% of the full radius) to be computed. A median distribution was calculated and plotted for each genotype.

Measurement of vessel length in adult retinas (using mice aged 4 to 13 months, including males and females, with similar age/sex distribution between the two genotypes) was carried out on maximal intensity projection images of individual retinal layers, by applying the NeuronJ plug-in in ImageJ (normally designed to trace axons) (Popko et al., 2009). For images of a fixed size, the total length was calculated by addition of all measured distances. Other measurements (number and type of intersections) were taken manually.

Statistics

All measurements above led to retrieving one numerical value per mouse or embryo (measured value, ratio or percentage). This allowed comparisons between two groups (genotypes). Sample size corresponds to the number of independent animals included in each group. No specific method was used to define sample size. Overall, sample groups include between seven and 15 individuals per genotype. For embryos and neonates, all individuals (littermates) obtained from the crosses initially set up were genotyped and all relevant genotypes were included. For these comparisons, statistical significance was evaluated using either the unpaired Student's *t*-test, when data were showing a normal distribution and equal variance, or the non-

parametric Mann-Whitney test (see figure legends). Differences were considered significant when $P<0.05$. All P-values are indicated in the figures, except in Fig. 7C where $**P<0.001$. For signal intensity plots (Figs 4D and 6C, Fig. S5D), the curves show for each pixel coordinates the median values±s.d. (in light blue, or light red). For scatter plots, all individual data are plotted (one dot per mouse) and the median value is shown with a black bar.

Peer review history
The peer review history is available online at https://journals.biologists.com/dev/article-lookup/doi/10.1242/dev.192047.

References
Aranguren, X. L., Agirre, X., Beerens, M., Coppiello, G., Uriz, M., Vandersmissen, I., Benkheil, M., Panadero, J., Aguado, N., Pascual-Montano, A. et al. (2013). Unraveling a novel transcription factor code determining the human arterial-specific endothelial cell signature. *Blood* **122**, 3982-3992. doi:10.1182/blood-2013-02-483255

Blair, S. and McNeill, H. (2018). Big roles for Fat cadherins. *Curr. Opin. Cell Biol.* **51**, 73-80. doi:10.1016/j.ceb.2017.11.006

Bovolenta, P. and Martinez-Morales, J.-R. (2019). Genetics of congenital eye malformations: insights from chick experimental embryology. *Hum. Genet.* **138**, 1001-1006. doi:10.1007/s00439-018-1900-5

Bruder-Nascimento, T., Chinnasamy, P., Riascos-Bernal, D. F., Cau, S. B., Callera, G. E., Touyz, R. M., Tostes, R. C. and Sibinga, N. E. S. (2014). Angiotensin II induces Fat1 expression/activation and vascular smooth muscle cell migration via Nox1-dependent reactive oxygen species generation. *J. Mol. Cell. Cardiol.* **66**, 18-26. doi:10.1016/j.yjmcc.2013.10.013

Cao, L. L., Riascos-Bernal, D. F., Chinnasamy, P., Dunaway, C. M., Hou, R., Pujato, M. A., O'Rourke, B. P., Miskolci, V., Guo, L., Hodgson, L. et al. (2016). Control of mitochondrial function and cell growth by the atypical cadherin Fat1. *Nature* **539**, 575-578. doi:10.1038/nature20170

Caruso, N., Herberth, B., Bartoli, M., Puppo, F., Dumonceaux, J., Zimmermann, A., Denadai, S., Lebosse, M., Roche, S., Geng, L. et al. (2013). Deregulation of the protocadherin gene FAT1 alters muscle shapes: implications for the pathogenesis of facioscapulohumeral dystrophy. *PLoS Genet.* **9**, e1003550. doi:10.1371/journal.pgen.1003550

Chang, L., Blain, D., Bertuzzi, S. and Brooks, B. P. (2006). Uveal coloboma: clinical and basic science update. *Curr. Opin Ophthalmol.* **17**, 447-470. doi:10.1097/01.icu.0000243020.82380.f6

Ciani, L., Patel, A., Allen, N. D. and Ffrench-Constant, C. (2003). Mice lacking the giant protocadherin mFAT1 exhibit renal slit junction abnormalities and a partially penetrant cyclopia and anophthalmia phenotype. *Mol. Cell. Biol.* **23**, 3575-3582. doi:10.1128/MCB.23.10.3575-3582.2003

Cirone, P., Lin, S., Griesbach, H. L., Zhang, Y., Slusarski, D. C. and Crews, C. M. (2008). A role for planar cell polarity signaling in angiogenesis. *Angiogenesis* **11**, 347-360. doi:10.1007/s10456-008-9116-2

Clements, R., Turk, R., Campbell, K. P. and Wright, K. M. (2017). Dystroglycan maintains inner limiting membrane integrity to coordinate retinal development. *J. Neurosci.* **37**, 8559-8574. doi:10.1523/JNEUROSCI.0946-17.2017

Davey, C. F. and Moens, C. B. (2017). Planar cell polarity in moving cells: think globally, act locally. *Development* **144**, 187-200. doi:10.1242/dev.122804

Duan, L. J., Takeda, K. and Fong, G. H. (2014). Hypoxia inducible factor-2α regulates the development of retinal astrocytic network by maintaining adequate supply of astrocyte progenitors. *PLoS ONE* **9**, e84736. doi:10.1371/journal.pone.0084736

Duan, L.-J., Pan, S. J., Sato, T. N. and Fong, G.-H. (2017). Retinal angiogenesis regulates astrocytic differentiation in neonatal mouse retinas by oxygen dependent mechanisms. *Sci. Rep.* **7**, 17608. doi:10.1038/s41598-017-17962-2

Edwards, M. M., Mammadova-Bach, E., Alpy, F., Klein, A., Hicks, W. L., Roux, M., Simon-Assmann, P., Smith, R. S., Orend, G., Wu, J. et al. (2010). Mutations in Lama1 disrupt retinal vascular development and inner limiting membrane formation. *J. Biol. Chem.* **285**, 7697-7711. doi:10.1074/jbc.M109.069575

Edwards, M. M., McLeod, D. S., Grebe, R., Heng, C., Lefebvre, O. and Lutty, G. A. (2011). Lama1 mutations lead to vitreoretinal blood vessel formation, persistence of fetal vasculature, and epiretinal membrane formation in mice. *BMC Dev. Biol.* **11**, 60. doi:10.1186/1471-213X-11-60

Fan, Y., Richelme, S., Avazeri, E., Audebert, S., Helmbacher, F., Dono, R. and Maina, F. (2015). Tissue-specific gain of RTK signalling uncovers selective cell vulnerability during embryogenesis. *PLoS Genet.* **11**, e1005533. doi:10.1371/journal.pgen.1005533

Fruttiger, M., Calver, A. R., Kruger, W. H., Mudhar, H. S., Michalovich, D., Takakura, N., Nishikawa, S. and Richardson, W. D. (1996). PDGF mediates a neuron-astrocyte interaction in the developing retina. *Neuron* **17**, 1117-1131. doi:10.1016/S0896-6273(00)80244-5

Fuhrmann, S. (2010). Eye morphogenesis and patterning of the optic vesicle. *Curr. Top. Dev. Biol.* **93**, 61-84. doi:10.1016/B978-0-12-385044-7.00003-5

Gee, H. Y., Sadowski, C. E., Aggarwal, P. K., Porath, J. D., Yakulov, T. A., Schueler, M., Lovric, S., Ashraf, S., Braun, D. A., Halbritter, J. et al. (2016). FAT1 mutations cause a glomerulotubular nephropathy. *Nat. Commun.* **7**, 10822. doi:10.1038/ncomms10822

Gerhardt, H., Golding, M., Fruttiger, M., Ruhrberg, C., Lundkvist, A., Abramsson, A., Jeltsch, M., Mitchell, C., Alitalo, K., Shima, D. et al. (2003). VEGF guides angiogenic sprouting utilizing endothelial tip cell filopodia. *J. Cell Biol.* **161**, 1163-1177. doi:10.1083/jcb.200302047

Gnanaguru, G., Bachay, G., Biswas, S., Pinzón-Duarte, G., Hunter, D. D. and Brunken, W. J. (2013). Laminins containing the beta2 and gamma3 chains regulate astrocyte migration and angiogenesis in the retina. *Development* **140**, 2050-2060. doi:10.1242/dev.087817

Haigh, J. J., Morelli, P. I., Gerhardt, H., Haigh, K., Tsien, J., Damert, A., Miquerol, L., Muhlner, U., Klein, R., Ferrara, N. et al. (2003). Cortical and retinal defects caused by dosage-dependent reductions in VEGF-A paracrine signaling. *Dev. Biol.* **262**, 225-241. doi:10.1016/S0012-1606(03)00356-7

Halfter, W., Dong, S., Dong, A., Eller, A. W. and Nischt, R. (2008). Origin and turnover of ECM proteins from the inner limiting membrane and vitreous body. *Eye (Lond)* **22**, 1207-1213. doi:10.1038/eye.2008.19

Helmbacher, F. (2018). Tissue-specific activities of the Fat1 cadherin cooperate to control neuromuscular morphogenesis. *PLoS Biol.* **16**, e2004734. doi:10.1371/journal.pbio.2004734

Horne-Badovinac, S. (2017). Fat-like cadherins in cell migration-leading from both the front and the back. *Curr. Opin. Cell Biol.* **48**, 26-32. doi:10.1016/j.ceb.2017.04.003

Hou, R. and Sibinga, N. E. S. (2009). Atrophin proteins interact with the Fat1 cadherin and regulate migration and orientation in vascular smooth muscle cells. *J. Biol. Chem.* **284**, 6955-6965. doi:10.1074/jbc.M809333200

Hou, R., Liu, L., Anees, S., Hiroyasu, S. and Sibinga, N. E. S. (2006). The Fat1 cadherin integrates vascular smooth muscle cell growth and migration signals. *J. Cell Biol.* **173**, 417-429. doi:10.1083/jcb.200508121

Kautzman, A. G., Keeley, P. W., Nahmou, M. M., Luna, G., Fisher, S. K. and Reese, B. E. (2018). Sox2 regulates astrocytic and vascular development in the retina. *Glia* **66**, 623-636. doi:10.1002/glia.23269

Kelly, R., Alonso, S., Tajbakhsh, S., Cossu, G. and Buckingham, M. (1995). Myosin light chain 3F regulatory sequences confer regionalized cardiac and skeletal muscle expression in transgenic mice. *J. Cell Biol.* **129**, 383-396. doi:10.1083/jcb.129.2.383

Kelly, R. G., Zammit, P. S., Schneider, A., Alonso, S., Biben, C. and Buckingham, M. E. (1997). Embryonic and fetal myogenic programs act through separate enhancers at the MLC1F/3F locus. *Dev. Biol.* **187**, 183-199. doi:10.1006/dbio.1997.8577

Kim, J., Kim, Y. H., Park, D. Y., Bae, H., Lee, D. H., Kim, K. H., Hong, S. P., Jang, S. P., Kubota, Y., Kwon, Y.-G. et al. (2017). YAP/TAZ regulates sprouting angiogenesis and vascular barrier maturation. *J. Clin. Invest.* **127**, 3441-3461. doi:10.1172/JCI93825

Lahrouchi, N., George, A., Ratbi, I., Schneider, R., Elalaoui, S. C., Moosa, S., Bharti, S., Sharma, R., Abu-Asab, M., Onojafe, F. et al. (2019). Homozygous frameshift mutations in FAT1 cause a syndrome characterized by colobomatous-microphthalmia, ptosis, nephropathy and syndactyly. *Nat. Commun.* **10**, 1180. doi:10.1038/s41467-019-08547-w

Lamballe, F., Genestine, M., Caruso, N., Arce, V., Richelme, S., Helmbacher, F. and Maina, F. (2011). Pool-specific regulation of motor neuron survival by

neurotrophic support. *J. Neurosci.* **31**, 11144-11158. doi:10.1523/JNEUROSCI. 2198-11.2011

Lavina, B., Castro, M., Niaudet, C., Cruys, B., Alvarez-Aznar, A., Carmeliet, P., Bentley, K., Brakebusch, C., Betsholtz, C. and Gaengel, K. (2018). Defective endothelial cell migration in the absence of Cdc42 leads to capillary-venous malformations. *Development* **145**, dev161182. doi:10.1242/dev.161182

Leighton, P. A., Mitchell, K. J., Goodrich, L. V., Lu, X., Pinson, K., Scherz, P., Skarnes, W. C. and Tessier-Lavigne, M. (2001). Defining brain wiring patterns and mechanisms through gene trapping in mice. *Nature* **410**, 174-179. doi:10.1038/35065539

Luo, L., Ambrozkiewicz, M. C., Benseler, F., Chen, C., Dumontier, E., Falkner, S., Furlanis, E., Gomez, A. M., Hoshina, N., Huang, W.-H. et al. (2020). Optimizing nervous system-specific gene targeting with Cre driver lines: prevalence of germline recombination and influencing factors. *Neuron* **106**, 37-65.e35. doi:10.1016/j.neuron.2020.01.008

Mariot, V., Roche, S., Hourde, C., Portilho, D., Sacconi, S., Puppo, F., Duguez, S., Rameau, P., Caruso, N., Delezoide, A. L. et al. (2015). Correlation between low FAT1 expression and early affected muscle in facioscapulohumeral muscular dystrophy. *Ann. Neurol.* **78**, 387-400. doi:10.1002/ana.24446

Mayor, R. and Etienne-Manneville, S. (2016). The front and rear of collective cell migration. *Nat. Rev. Mol. Cell Biol.* **17**, 97-109. doi:10.1038/nrm.2015.14

Morcillo, J., Martínez-Morales, J. R., Trousse, F., Fermin, Y., Sowden, J. C. and Bovolenta, P. (2006). Proper patterning of the optic fissure requires the sequential activity of BMP7 and SHH. *Development* **133**, 3179-3190. doi:10.1242/dev.02493

Morita, A., Ushikubo, H., Mori, A., Arima, S., Sakamoto, K., Nagamitsu, T., Ishii, K. and Nakahara, T. (2017). A delay in vascularization induces abnormal astrocyte proliferation and migration in the mouse retina. *Dev. Dyn.* **246**, 186-200. doi:10.1002/dvdy.24484

Morley, S. J., Qi, Y., Iovino, L., Andolfi, L., Guo, D., Kalebic, N., Castaldi, L., Tischer, C., Portulano, C., Bolasco, G. et al. (2016). Acetylated tubulin is essential for touch sensation in mice. *eLife* **5**, e20813. doi:10.7554/eLife.20813

Morris, L. G. T., Kaufman, A. M., Gong, Y., Ramaswami, D., Walsh, L. A., Turcan, Ş., Eng, S., Kannan, K., Zou, Y., Peng, L. et al. (2013). Recurrent somatic mutation of FAT1 in multiple human cancers leads to aberrant Wnt activation. *Nat. Genet.* **45**, 253-261. doi:10.1038/ng.2538

Moutin, M. J., Bosc, C., Peris, L. and Andrieux, A. (2021). Tubulin post-translational modifications control neuronal development and functions. *Dev. Neurobiol.* **81**, 253-272. doi:10.1002/dneu.22774

Nakajima, H., Yamamoto, K., Agarwala, S., Terai, K., Fukui, H., Fukuhara, S., Ando, K., Miyazaki, T., Yokota, Y., Schmelzer, E. et al. (2017). Flow-dependent endothelial YAP regulation contributes to vessel maintenance. *Dev. Cell* **40**, 523-536.e26. doi:10.1016/j.devcel.2017.02.019

O'Sullivan, M. L., Punal, V. M., Kerstein, P. C., Brzezinski, J. A., IV, Glaser, T., Wright, K. M. and Kay, J. N. (2017). Astrocytes follow ganglion cell axons to establish an angiogenic template during retinal development. *Glia* **65**, 1697-1716. doi:10.1002/glia.23189

Paredes, I., Himmels, P. and Ruiz de Almodovar, C. (2018). Neurovascular communication during CNS development. *Dev. Cell* **45**, 10-32. doi:10.1016/ j.devcel.2018.01.023

Popko, J., Fernandes, A., Brites, D. and Lanier, L. M. (2009). Automated analysis of NeuronJ tracing data. *Cytometry A* **75A**, 371-376. doi:10.1002/cyto.a.20660

Puppo, F., Dionnet, E., Gaillard, M.-C., Gaildrat, P., Castro, C., Vovan, C., Bertaux, K., Bernard, R., Attarian, S., Goto, K. et al. (2015). Identification of variants in the 4q35 gene FAT1 in patients with a facioscapulohumeral dystrophy-like phenotype. *Hum. Mutat.* **36**, 443-453. doi:10.1002/humu.22760

Quaegebeur, A., Lange, C. and Carmeliet, P. (2011). The neurovascular link in health and disease: molecular mechanisms and therapeutic implications. *Neuron* **71**, 406-424. doi:10.1016/j.neuron.2011.07.013

Rattner, A., Williams, J. and Nathans, J. (2019). Roles of HIFs and VEGF in angiogenesis in the retina and brain. *J. Clin. Invest.* **129**, 3807-3820. doi:10.1172/ JCI126655

Rivers, L. E., Young, K. M., Rizzi, M., Jamen, F., Psachoulia, K., Wade, A., Kessaris, N. and Richardson, W. D. (2008). PDGFRA/NG2 glia generate myelinating oligodendrocytes and piriform projection neurons in adult mice. *Nat. Neurosci.* **11**, 1392-1401. doi:10.1038/nn.2220

Ruhrberg, C. and Bautch, V. L. (2013). Neurovascular development and links to disease. *Cell. Mol. Life Sci.* **70**, 1675-1684. doi:10.1007/s00018-013-1277-5

Sadeqzadeh, E., de Bock, C. E. and Thorne, R. F. (2014). Sleeping giants: emerging roles for the fat cadherins in health and disease. *Med. Res. Rev.* **34**, 190-221. doi:10.1002/med.21286

Sakabe, M., Fan, J., Odaka, Y., Liu, N., Hassan, A., Duan, X., Stump, P., Byerly, L., Donaldson, M., Hao, J. et al. (2017). YAP/TAZ-CDC42 signaling regulates vascular tip cell migration. *Proc. Natl. Acad. Sci. USA* **114**, 10918-10923. doi:10.1073/pnas.1704030114

Selvam, S., Kumar, T. and Fruttiger, M. (2018). Retinal vasculature development in health and disease. *Prog. Retin. Eye Res.* **63**, 1-19. doi:10.1016/j.preteyeres. 2017.11.001

Shue, E. H., Carson-Walter, E. B., Liu, Y., Winans, B. N., Ali, Z. S., Chen, J. and Walter, K. A. (2008). Plasmalemmal vesicle associated protein-1 (PV-1) is a marker of blood-brain barrier disruption in rodent models. *BMC Neurosci.* **9**, 29. doi:10.1186/1471-2202-9-29

Srinivas, S., Watanabe, T., Lin, C.-S., William, C. M., Tanabe, Y., Jessell, T. M. and Costantini, F. (2001). Cre reporter strains produced by targeted insertion of EYFP and ECFP into the ROSA26 locus. *BMC Dev. Biol.* **1**, 4. doi:10.1186/1471-213X-1-4

Stan, R. V., Tkachenko, E. and Niesman, I. R. (2004). PV1 is a key structural component for the formation of the stomatal and fenestral diaphragms. *Mol. Biol. Cell* **15**, 3615-3630. doi:10.1091/mbc.e03-08-0593

Stefater, J. A., III, Lewkowich, I., Rao, S., Mariggi, G., Carpenter, A. C., Burr, A. R., Fan, J., Ajima, R., Molkentin, J. D., Williams, B. O. et al. (2011). Regulation of angiogenesis by a non-canonical Wnt-Flt1 pathway in myeloid cells. *Nature* **474**, 511-515. doi:10.1038/nature10085

Stone, J., Itin, A., Alon, T., Pe'er, J., Gnessin, H., Chan-Ling, T. and Keshet, E. (1995). Development of retinal vasculature is mediated by hypoxia-induced vascular endothelial growth factor (VEGF) expression by neuroglia. *J. Neurosci.* **15**, 4738-4747. doi:10.1523/JNEUROSCI.15-07-04738.1995

Sugiyama, Y., Shelley, E. J., Badouel, C., McNeill, H. and McAvoy, J. W. (2015). Atypical cadherin Fat1 is required for lens epithelial cell polarity and proliferation but not for fiber differentiation. *Invest. Ophthalmol. Vis. Sci.* **56**, 4099-4107. doi:10.1167/iovs.15-17008

Tao, C. and Zhang, X. (2014). Development of astrocytes in the vertebrate eye. *Dev. Dyn.* **243**, 1501-1510. doi:10.1002/dvdy.24190

Tao, C. and Zhang, X. (2016). Retinal proteoglycans act as cellular receptors for basement membrane assembly to control astrocyte migration and angiogenesis. *Cell Rep.* **17**, 1832-1844. doi:10.1016/j.celrep.2016.10.035

Tronche, F., Kellendonk, C., Kretz, O., Gass, P., Anlag, K., Orban, P. C., Bock, R., Klein, R. and Schütz, G. (1999). Disruption of the glucocorticoid receptor gene in the nervous system results in reduced anxiety. *Nat. Genet.* **23**, 99-103. doi:10.1038/12703

Wang, X., Freire Valls, A., Schermann, G., Shen, Y., Moya, I. M., Castro, L., Urban, S., Solecki, G. M., Winkler, F., Riedemann, L. et al. (2017). YAP/TAZ orchestrate VEGF signaling during developmental angiogenesis. *Dev. Cell* **42**, 462-478.e67. doi:10.1016/j.devcel.2017.08.002

Watanabe, T. and Raff, M. C. (1988). Retinal astrocytes are immigrants from the optic nerve. *Nature* **332**, 834-837. doi:10.1038/332834a0

West, H., Richardson, W. D. and Fruttiger, M. (2005). Stabilization of the retinal vascular network by reciprocal feedback between blood vessels and astrocytes. *Development* **132**, 1855-1862. doi:10.1242/dev.01732

Williamson, K. A., Rainger, J., Floyd, J. A. B., Ansari, M., Meynert, A., Aldridge, K. V., Rainger, J. K., Anderson, C. A., Moore, A. T., Hurles, M. E. et al. (2014). Heterozygous loss-of-function mutations in YAP1 cause both isolated and syndromic optic fissure closure defects. *Am. J. Hum. Genet.* **94**, 295-302. doi:10.1016/j.ajhg.2014.01.001
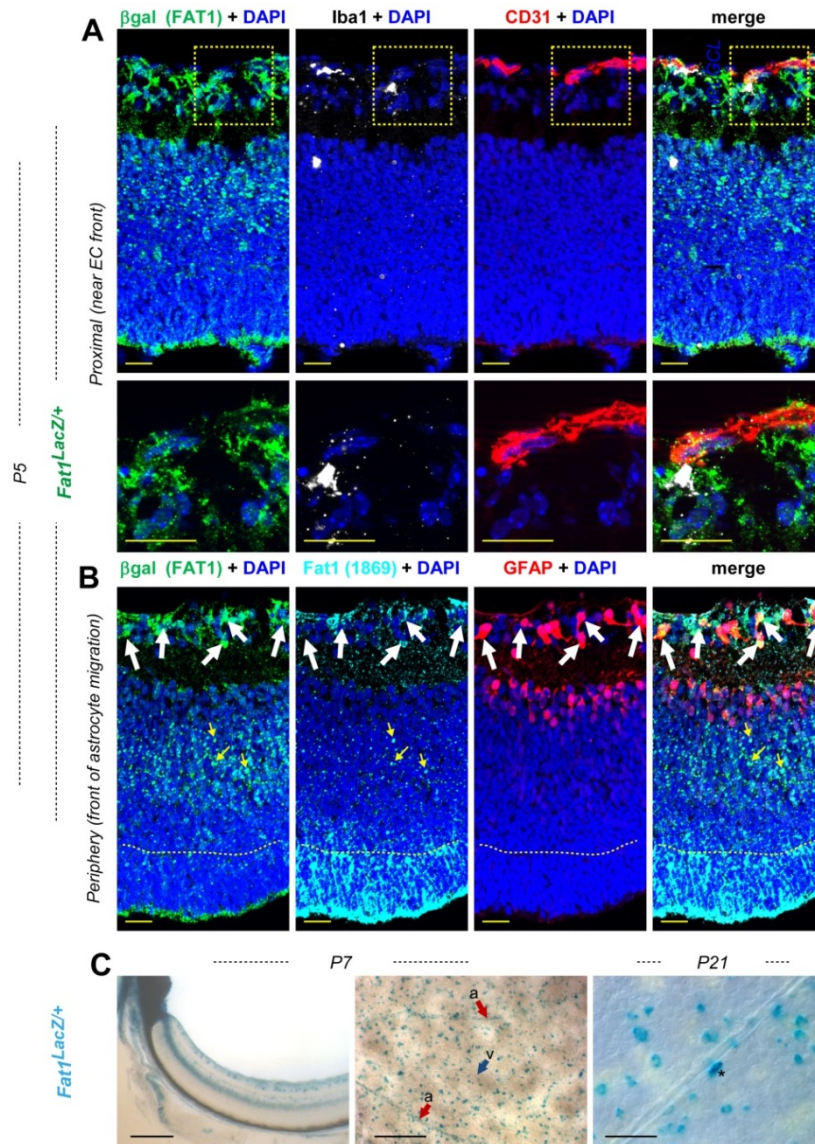
Fig. S1. Complementary analysis of *Fat1* expression using the *Fat1^LacZ^* reporter allele in retinas from P5, P7, and P21 mice. (A, B) Analysis by IHC on cross-sections of P5 *Fat1^LacZ^* retinas was carried on with antibodies against β-galactosidase (green, A, B), CD31 (red, A), IBA1 (white, A), PDGFRα (red, B) and FAT1 (Cyan, B). Cell nuclei were labeled with DAPI. The bottom row panels in (A) show high magnification of the regions highlighted with yellow-dotted areas, focusing on endothelial cells and microglia, exhibiting low FAT1/ β-galactosidase levels, relative to nearby astrocytes. In (B), the apparent discrepancy between β-galactosidase

and FAT1 localisation likely reflects the fact that the mutant fusion protein (detected by both antibodies) is retained in the secretory pathway, whereas only the wild-type protein reaches the membrane, thus decorating apical ends of Mueller glia, as well as light-receiving segments of rods and cones. (C) β-galactosidase activity is detected in P7 and P27 *Fat1^{LacZ}* retinas by X-gal staining. Flat mounted presentations allow detecting signal in scattered cells throughout the RGC layer, as well as along arteries (a) but not veins (v). Scale bars: (A, B): 20µm (C) P7: 200µm; P21: 50µm.
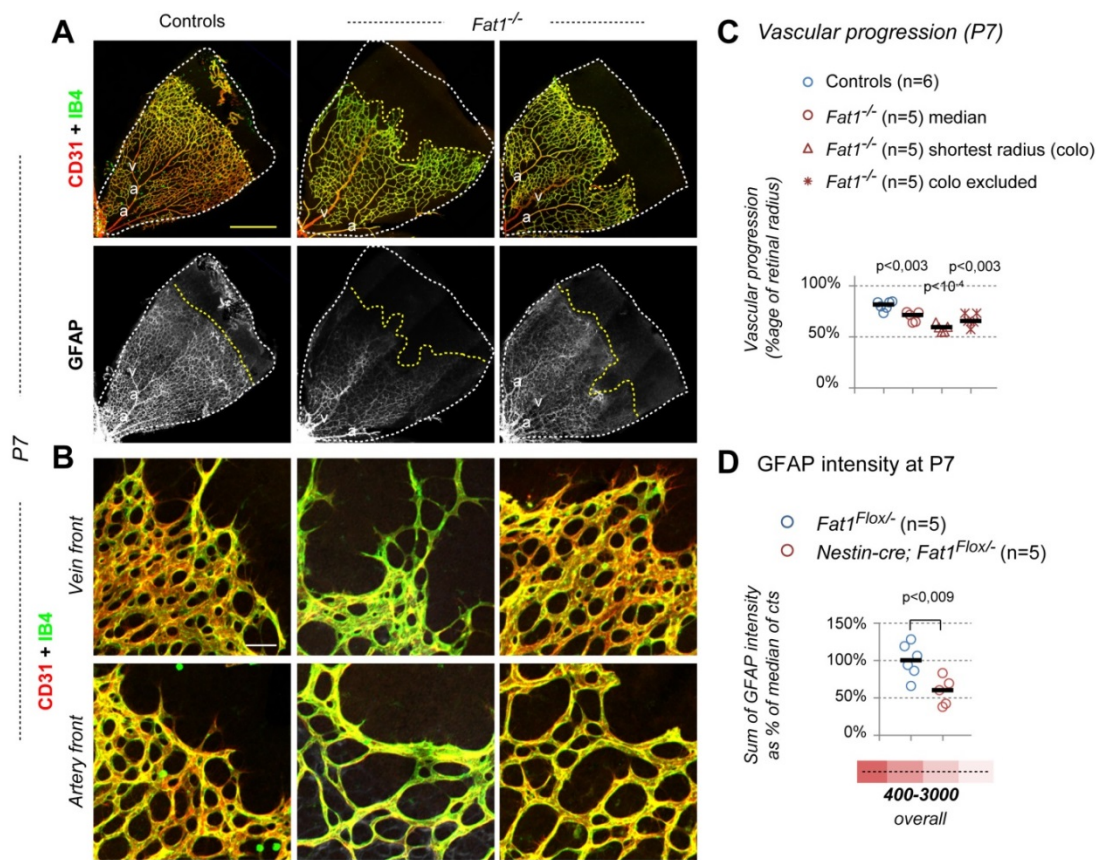
Fig. S2. Constitutive Fat1 disruption impairs vascular progression p. (A, B) Flat mounted retinas from Wild type control, and two examples of *Fat1⁻/⁻* mutant pups at P7, after immunohistochemistry with the GS-IB4 lectin (green), and antibodies against CD31 (red), and GFAP (white). Images in (A) feature an entire quadrant of retina; Lower pictures in (B) correspond high magnification views of the vascular front, in areas perfused by vessels connected to the nearest vein (top) or artery (bottom), respectively, showing the difference in EC density. (C) quantifications of the distance covered by IB4-positive ECs along the center-to-periphery axis, relative to the retinal radius at P7, distinguishing quadrants with minimal radius (with coloboma), from normally sized quadrants. (D) The intensity of GFAP staining was quantified along the radius was measured in control and *Nestin-cre; Fat1^Flox/-^* mutants retinas at P7, and the sum of signal intensity was calculated for a window spanning the distances schematically represented corresponding to images shown in Fig. 4B. Scale bars: (A): 500μm (B) 50μm.
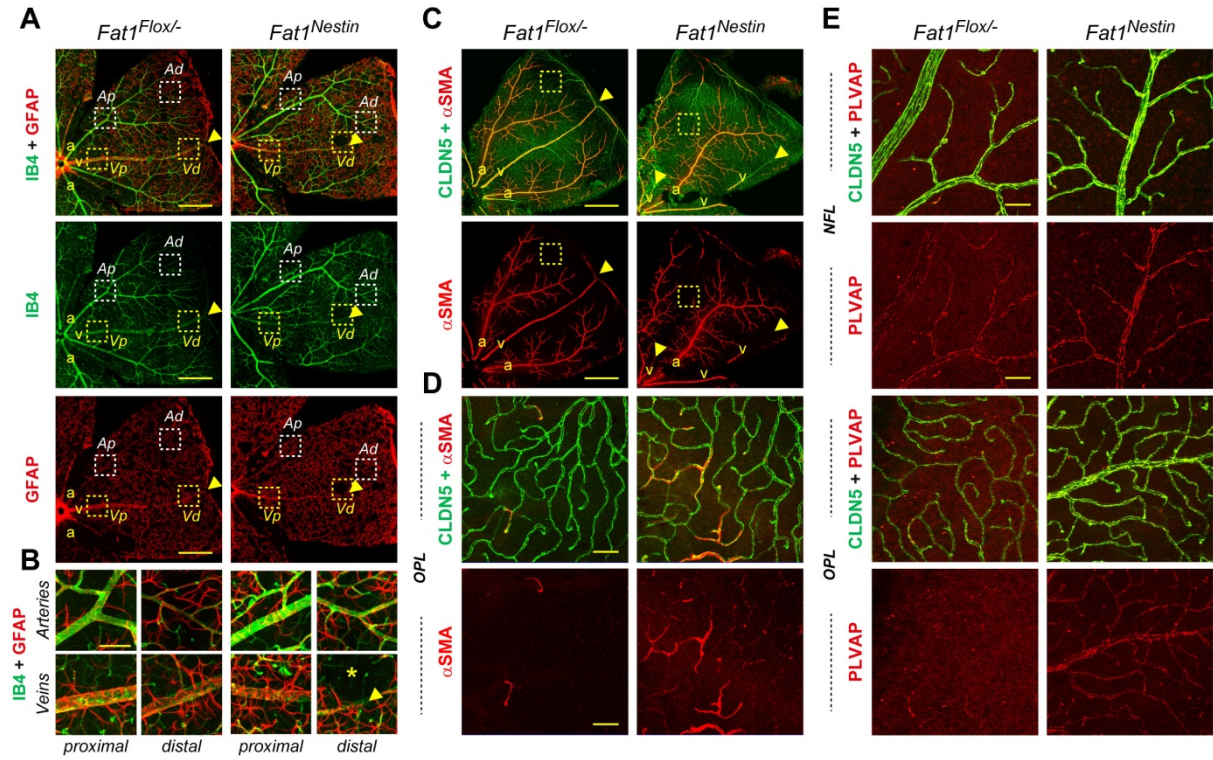
Fig. S3. Adult mice with neural Fat1 ablation exhibit disrupted blood brain barrier. (A) Images of flat-mounted retinas immunostained with: (A, B) IB4 (green) and GFAP (red); (C, D) Claudin5 (Cldn5, green) and αSMA (Acta2, red); (E) Cldn5 (green) and PLVAP (red), visualizing either a quadrant (A, C), or regions highlighted in (A, C) with yellow-dotted squares. Scale bars: (A, C) 500μm; (B): 100μm; (D, E): 50μm.
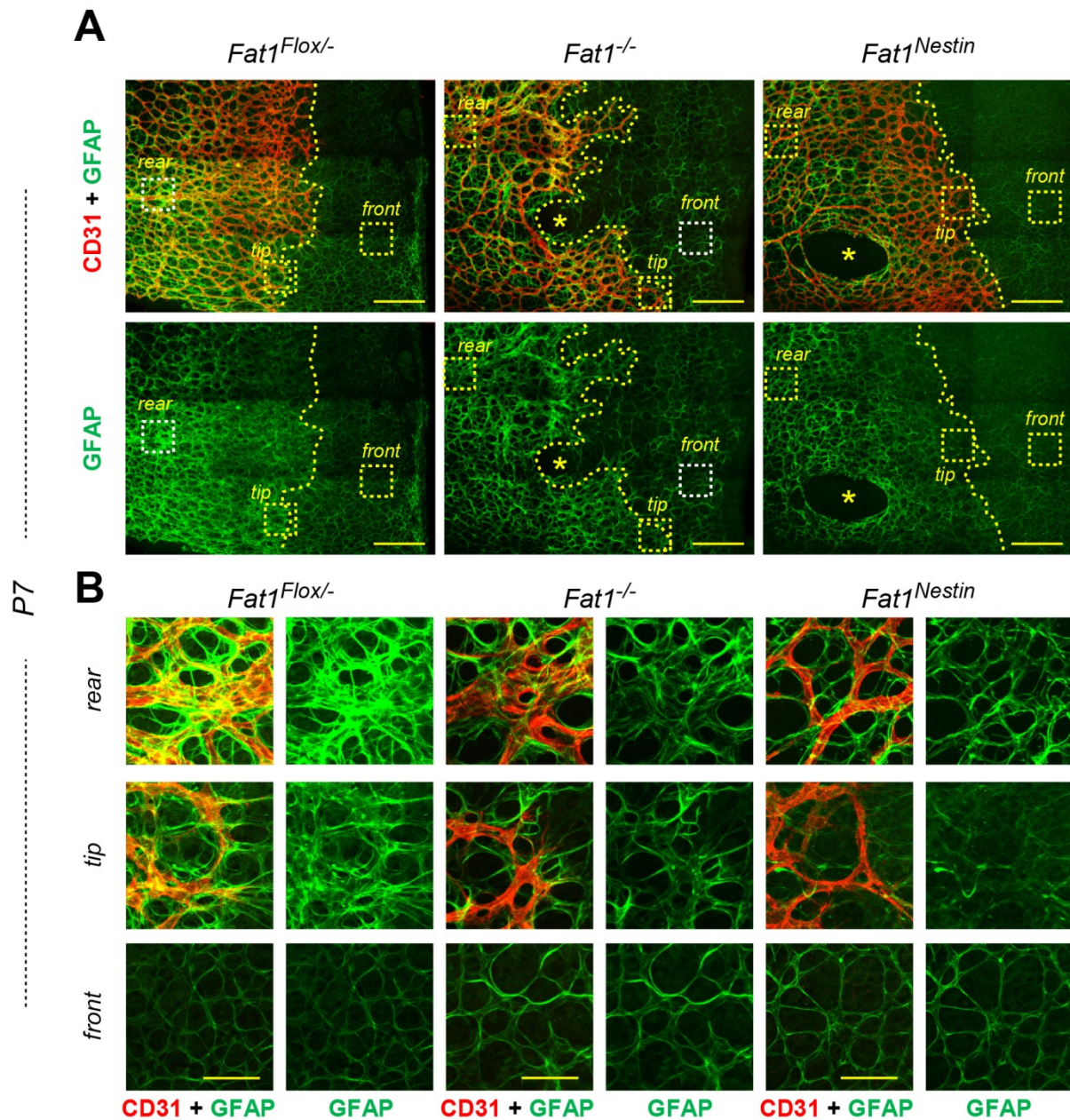
Fig. S4. *Fat1* **ablation in the neural lineage alters astrocyte maturation.** Flat-mounted retinas from *Fat1*^{*Flox/-*} control, *Fat1*^{*-/-*} and *Fat1*^{*Nestin*} mutant pups at P7 after immunostaining with antibodies against CD31 (red) and against GFAP (green). Upper pictures (A) represent an area of the retina spanning from near the center (to the left), where the astrocyte layer is covered by endothelial cells, to the distal most part of the retina (to the right), where GFAP levels are low in absence of vascular coverage. Lower pictures in (B) correspond to the dotted boxes highlighted in (A), visualizing for each genotype, a region 1) in the vascularized area (rear); 2) at the level of tip endothelial cells (tip); and 3) in the "avascular" distal region (front). Scale bars: (A) 200μm, (B) 50μm.
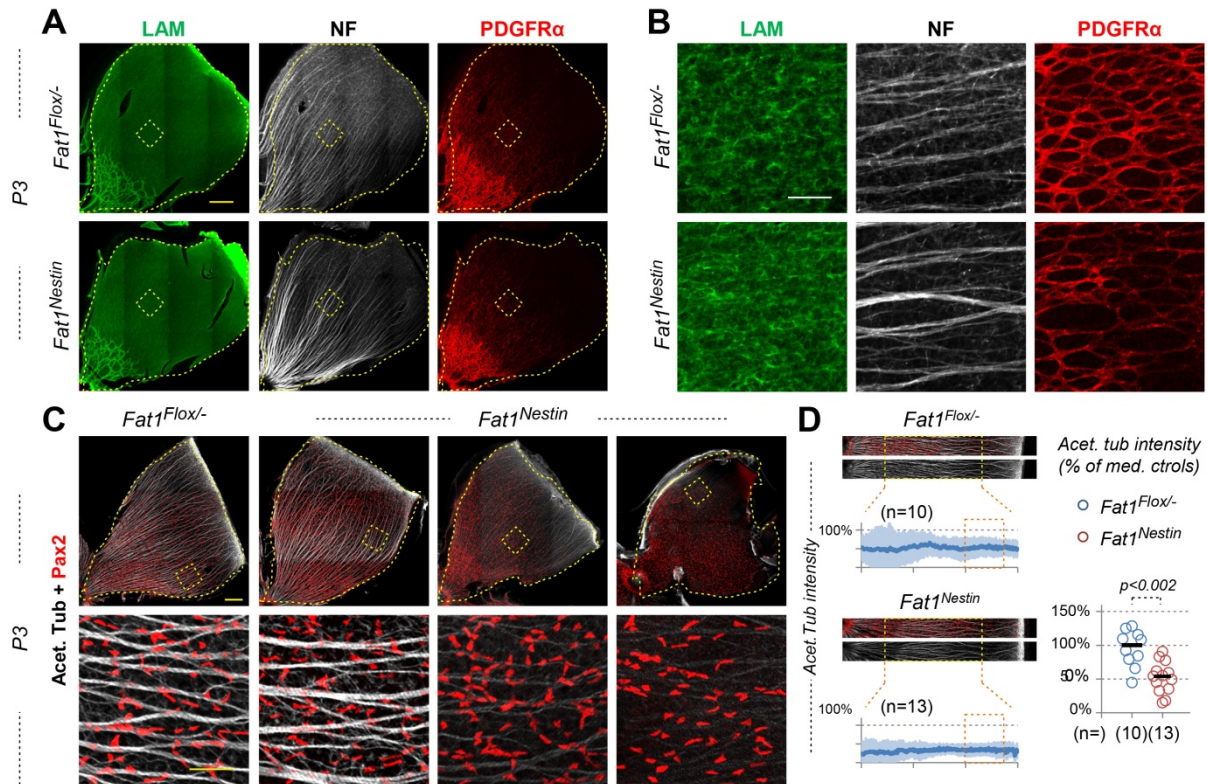
Fig. S5. Normal ILM and RGC axon trajectories. Flat-mounted retinas from P3 *Fat1^Flox/-* control, *Fat1^-/-* and *Fat1^Nestin* mice after immunostaining with antibodies against (A, B): Laminin (green), Neurofilament (white) PDGFRa (red); and (C,D) against PAX2 (red), and Acetylated Tubulin (white). Panels in (B) and lower images in (C) correspond to the dotted boxes highlighted in (A) and in (C), respectively. (D) quantification of signal intensity along windows spanning along the center-periphery radius. Scale bars: (A, C top panels): 200µm; (B, C bottom panels) 50µm.
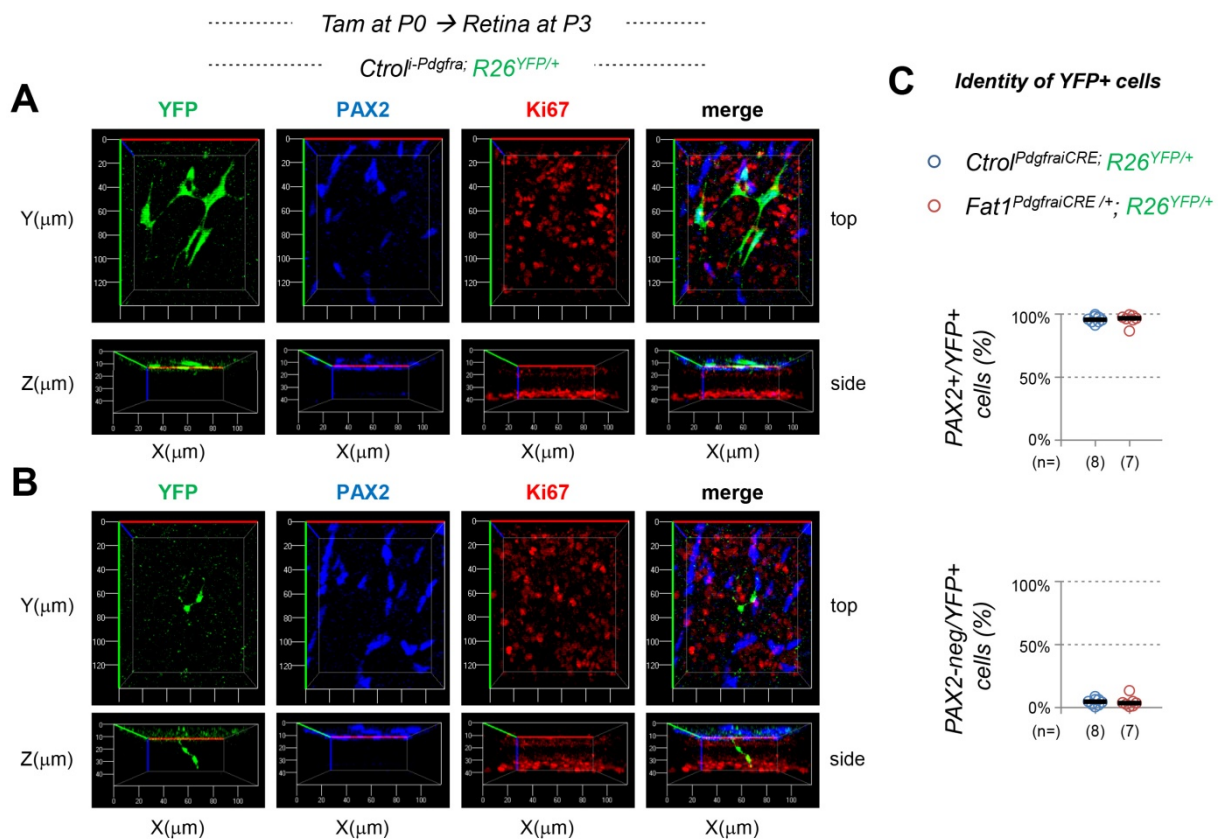
Fig. S6. The Pdgfra-iCRE driver predominantly targets migrating astrocytes in the postnatal retina. (A, B) Imaging through the full depth of a retina from a $Ctrol^{Pdgfra-iCRE}$ mouse injected with Tamoxifen at P0, and collected at P3 and stained with GFP (green), PAX2 (blue) and Ki67 (as in Fig. 8), showing for two different regions (A, B), a Maximal intensity projection from the top (Y and Z axes, top images), and a Z-view (Z/X bottom images). Ki67 predominantly labels deep cells (future rods & cones), whereas PAX2+ astrocytes decorate the inner most layer. (A) Most YFP+ cells correspond to PAX2+ astrocytes, positioned in the inner layer. (B) A small fraction of YFP+ cells are sometimes located in deeper layers, and do not co-express PAX2. (C) Quantifications of the respective percentages of PAX2+ (top) and PAX2-negative (bottom) cells among YFP+ cells in $Ctrol^{Pdgfra-iCRE}$ (blue dots) and $Fat1^{Pdgfra-iCRE}$ mice (red dots). This shows that CRE-mediated excision predominantly occurs in astrocytes, with only marginal activity in other cells (2-5% of all YFP$^+$ cells). PAX2-negative/YFP$^+$ cells were not included in quantifications shown in Fig. 8. Scatter plots: data from individual mice, with thick black lines marking median values ($Ctrol^{Pdgfra-iCRE}$ (n=8), and $Fat1^{Pdgfra-iCRE}$ (n=7)). Scale bars: (A, B): depth (Z axis) 40µm; Width (X axis): 100µm.
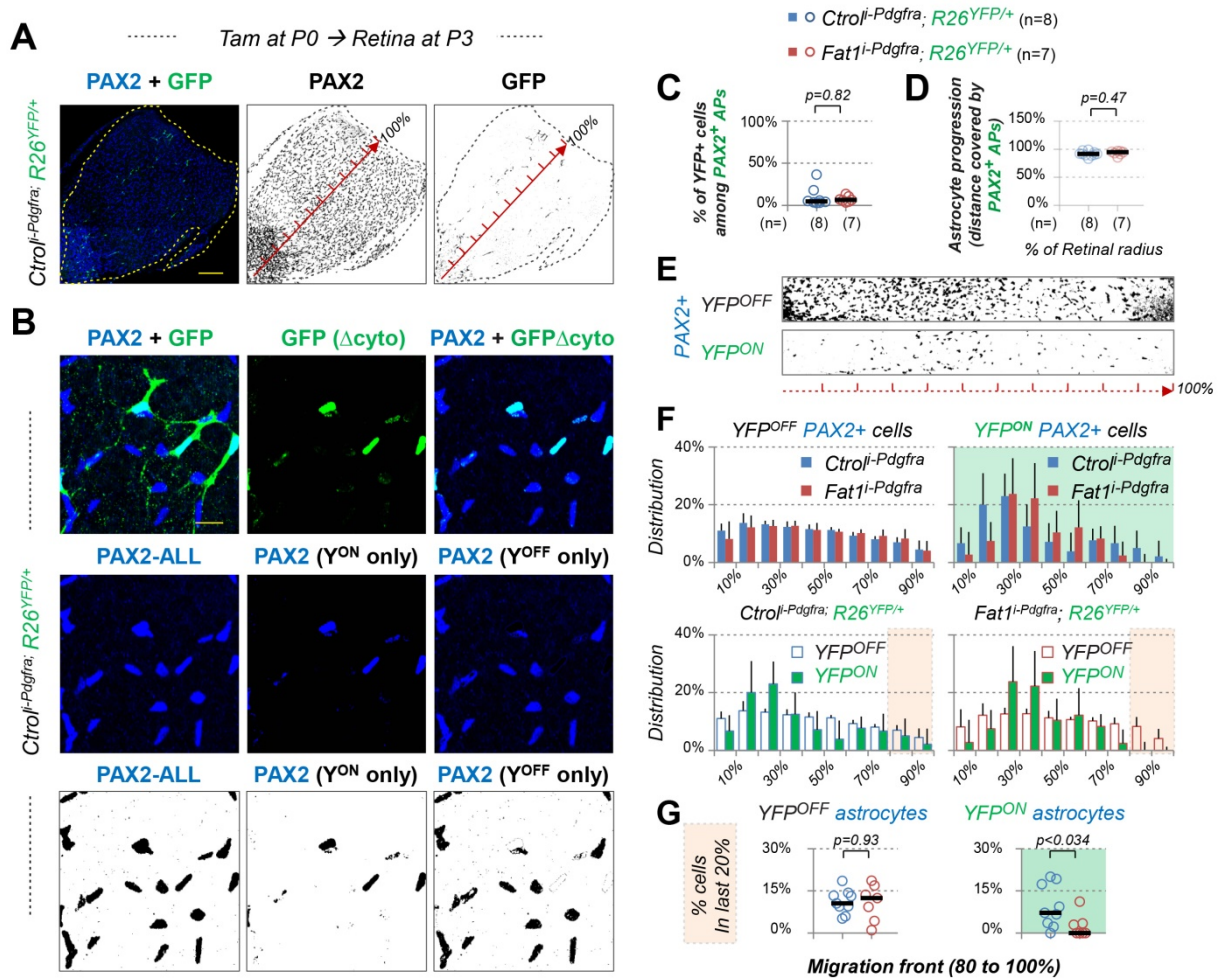
Fig. S7. Recombination efficacy of the Pdgfra-iCRE driver is limited to a small proportion of retinal astrocytes, insufficient to affect progression of non-recombined astrocytes. (A, B) Flat-mounted P3 retinas from a *Ctrol^Pdgfra-iCRE* mouse previously injected with Tamoxifen at P0, stained with (A, B) GFP (green), and PAX2 antibodies shown as merged colours or thresholded black and white images, showing a full retinal quadrant (A), or a high magnification of a small area (B). Images in (B) show the image processing steps used for selection in the PAX2 channel of YFP-positive or negative astrocytes, for conversion into thresholded images (bottom), used for subsequent image analyses. (C-G) Quantifications of recombination efficiency and morphometric analyses of Astrocyte phenotypes in *Ctrol^Pdgfra-iCRE* and *Fat1^Pdgfra-iCRE* retinas: (C) Percentages of recombined astrocytes (YFP$^+$, among PAX2$^+$ cells) ; (D) Overall astrocyte progression across the retinal radius; (E) Example of thresholded images of area spanning a retinal radius, where YFP^{ON} and YFP^{OFF} PAX2$^+$ astrocytes are analyzed; (F) Distribution analyses of YFP^{ON} and YFP^{OFF} PAX2$^+$ astrocytes in *Ctrol^Pdgfra-iCRE* and *Fat1^Pdgfra-iCRE* retinas; (G) Percentages of YFP^{ON} (left plot) and YFP^{OFF} (right plot) PAX2+ astrocytes observed in the last 20% of the astrocyte span, showing no phenotype in non-recombined astrocytes, whereas YFP$^+$-recombined astrocytes are affected by *Fat1* deletion. Statistics: p-values were calculated using unpaired two-sided Student test, assuming unequal variance. Scale bars: (A): 200μm; (B): 20μm.

Table S1. Mouse lines

#	Line name	Mouse Genome informatics (MGI) name/page link	1st reference	PMID with Link	Type of genetic mofication	Locus	Comments	How it is used in this study
1	Fat1-Flox	Fat1tm1.1Fhel	Caruso et al., Plos Genetics 2013	23785297	conditional allele	Fat1	Exons 24 and 25, encoding the transmembrane domain of Fat1, were Flanked by LoxP sites. An FRT-flanked neo cassette has been deleted.	conditional analysis of Fat1 function
2	Fat1-KO	Fat1tm1.2Fhel	Caruso et al., Plos Genetics 2013	23785297	knockout allele (derived from the Fat1 Flox allele)	Fat1	This allele is derived from the Fat1-Flox allele by constitutive deletion of the Floxed cassette using a Deleter-cre line. The resulting protein lacks a transmembrane domain, but remains found in membrane fractions. This allele is a null allele	Fat1 knockout phenotypes
3	Fat1-LacZ	Fat1Gt(KST249)Byg	Stryke et al., Nucl. Ac. Res. 2003; Caruso et al., Plos Genetics 2013	23785297	Genetrap (knock-in/knock-out)	Fat1	A gene-trap construct (splice acceptor, transmembrane domain and beta-galactosidase, followed by a poly A plus an FRT-flanked Alcaline Phosphatase) was inserted in the Fat1 locus, downstream of exon1, which encodes the first 8 cadherin domains of Fat1 extracellular domain. The resulting Fat1-LacZ fusion protein is non-functional.	LacZ expression is used as a reporter of Fat1 expression
4	Nestin-cre	Tg(Nes-cre)1Kln	Tronche F, et al., Nat Genet. 1999	10471508	transgenic	Not identified (Chr 3)	This transgene expresses Cre recombinase driven by regulatory regions of the a rat nestin (Nes) gene, including the promoter and a nervous system-specific enhancer present in the second intron. This transgene allows Cre expression in neuronal and glial cell precursors.	Cre expression in the neural lineage, with late onset in the retina.
6	pdgfra-cre/ERT2	Tg(Pdgfra-cre/ERT2)1Wdr	Rivers LE, et al., Nat. Neurosci. 2008	18849983	BAC transgenic	not identified	A mouse PAC clone (RPCI21-546M3) containing the Pdgfra gene was modified by inserting the Tamoxifen-inducible Cre/ERT2 sequence at the ATG of pdgfra, in place of exon 1. This results in expression of Cre/ERT2 in the domain of pdgfra expression,	Tamoxifen-inducible CRE-mediated deletion in migrating retinal astrocytes
6	R26-YFP	Gt(ROSA)26Sortm1(EYFP)Cos	Srinivas S, et al., BMC Dev Biol 2001	11299042	Knock-in/knock-out	Rosa26 (Gt(ROSA)26)	The Rosa26 locus is ubiquitously expressed, and easily targetable, without phenotypical consequences. In this ligne, a Lox-STOP-Lox Cassette, followed by the YFP sequence, allows YFP to be expressed in any cell, after CRE-mediated recombination	Reporter of CRE mediated deletion (YFP positive cells)
7	MLC3F-2E-LavZ	Tg(Myl1-lacZ)1Ibdml	Kelly R, et al. J Cell Biol 1995	7721942	transgenic	not identified	In the transgenic construct, the 2E enhancer of the MLC3F gene was used to drive expression of an NLS-LacZ reporter (nuclear localised). Used as a muscle marker	Highlight muscles in embryos, Used here for positional information

Table S2. Antibodies and other reagent

Antibodies	provider	catalog number	Identifier (RRID)
Anti-PAX7 (supernatant) Mouse Monoclonal antibody	DSHB	PAX7 (supernatant)	**AB_2299243**
Anti-Neurofilament Mouse Monoclonal antibody, Clone 2H3 (bioreactor)	DSHB	2H3 (bioreactor)	**AB_531793**
Anti-Neurofilament Rabbit polyclonal Antibody	Millipore	Ab1987	**AB_91201**
Anti myosin heavy chain, type I (Myh1) Antibody, Mouse monoclonal, Clone MF20 (bioreactor)	DSHB	MF20 (bioreactor)	**AB_2147781**
Anti-β-galactosidase Rabbit polyclonal antibody	Abcam	ab9361	**AB_307210**
Anti-GFP Antibody, Rabbit Polyclonal	Aves	GFP-1020	**AB_10000240**
Mouse Anti-Human GLUL (Glutamine Synthetase (GS)) Monoclonal Antibody, Unconjugated, Clone 2B12	Novus	H00002752-M01A	**AB_1199735**
Mouse Anti-Glial Fibrillary Acidic Protein (GFAP) Monoclonal Antibody, Unconjugated, Clone G-A-5	SIGMA ALDRICH	G3893	**AB_477010**
Purified anti-Pax2 Rabbit polyclonal antibody	Covance	PRB-276P	**AB_291611**
Purified Rat anti-mouse CD140a (Pdgfrα) monoclonal antibody - clone APA5	BD Biosciences	558774	**AB_397117**
Rat anti-Mouse CD31 (PECAM) monoclonal antibody, Clone MEC13,3 (15.625 µg/ml)	BD Biosciences	550274	**AB_393571**
Rat anti-Mouse CD31 (PECAM) monoclonal antibody, Clone MEC13,3 (0.5 mg/ml)	BD Biosciences	550274	**AB_394816**
Anti-alpha, smooth muscle actin (Acta2), Rabbit monoclonal antibody (clone D4K9N)	Cell Signaling Technology	19245S	**AB_2734735**
Anti-Claudin 5 (CLDN5) Monoclonal Antibody (Clone 4C3C2), Alexa Fluor 488 conjugated	Thermofisher Scientific	352588	**AB_2532189**
Rat Anti-PLVAP (Panendothelial Cell Antigen) Monoclonal Antibody, Unconjugated, Clone MECA-32	BD Biosciences	553849	**AB_395086**
Anti-IBA1 Rabbit polyclonal Antibody	WAKO CHEMICALS	019-19741	**AB_839504**
Purified Mouse Anti-Ki-67	BD Biosciences	550609	**AB_393778**
Monoclonal anti-Acetylated Tubulin Antibody, clone 6-11B-1	SIGMA ALDRICH	T6793	**AB_477585**
Other reagents	**provider**	**catalog number**	**RRID**
Isolectin GS-IB$_4$ From *Griffonia simplicifolia*, Alexa Fluor™ 488 Conjugate	Thermofisher Scientific	I21411	**AB_2314662**
Prolong-Gold anti-fade Mountant, with DAPI (5x2ml)	Thermofisher Scientific	**P36935**	-